A Nanofabricated Amplitude-Division Electron Interferometer in a Transmission Electron Microscope

by

Akshay Agarwal

B.Tech., M.Tech. Electrical Engineering
IIT Bombay (2014)

Submitted to the Department of Electrical Engineering and Computer Science
in Partial Fulfillment of the Requirements for the Degree of

Master of Science in Electrical Engineering and Computer Science

at the

MASSACHUSETTS INSTITUTE OF TECHNOLOGY

September 2016



Signature redacted

Signature of Author.....

Department of Electrical Engineering and Computer Science
August 29, 2016

Signature redacted

Certified by.....

Karl K. Berggren
Professor of Electrical Engineering and Computer Science
Thesis Supervisor

Signature redacted

Accepted by.....

Leslie A. Kolodziejski
Professor of Electrical Engineering and Computer Science
Chair, Department Committee on Graduate Students

A Nanofabricated Amplitude-Division Electron Interferometer in a Transmission Electron Microscope

by

Akshay Agarwal

Submitted to the Department of Electrical Engineering and Computer Science on August 29, 2016 in Partial Fulfillment of the Requirements for the Degree of Master of Science in Electrical Engineering and Computer Science

ABSTRACT

Wavefront-division electron interferometry with the electron biprism has enabled many applications such as electron holography, exit-wave reconstruction, and demonstration of the Aharonov-Bohm effect. However, wavefront-division interferometry is limited by the requirement of high source coherence. Amplitude-division electron interferometers, first demonstrated by Marton and co-workers in 1954, can overcome this limitation. The implementation of these interferometers is hindered by the precise rotational and translational alignment required. This thesis develops a self-aligned, monolithic electron interferometer consisting of two 45 nm thick silicon layers separated by 20 μm and fabricated from a single crystal silicon cantilever on a transmission electron microscope grid by gallium focused ion-beam milling. Using this interferometer, beam path-separation and interference fringes of lattice periodicity and a maximum contrast of 15% in an unmodified 200 kV transmission electron microscope was demonstrated. This interferometer design can potentially be scaled to millimeter-scale and used in electron holography. It can also be applied to perform fundamental physics experiments such as interaction-free measurement with electrons, with the aim of significantly reducing the damage suffered by biological samples during high-resolution microscopy. Thus, the interferometer can serve as a proof-of-concept of the recently proposed 'Quantum Electron Microscope'.

Thesis Supervisor: Karl K. Berggren

Title: Professor of Electrical Engineering and Computer Science

# Acknowledgments

The work reported in this thesis would not have been possible without the constant support, encouragement and advice of my research supervisor, Prof. Karl K. Berggren. Karl was always approachable and open to all my questions and doubts. I sincerely appreciate his guidance which has contributed immensely towards improving my understanding of my research and making me a better scientist.

I would also like to thank Dr. Chung-Soo Kim for developing the fabrication process for the samples used in this thesis. Dr. Kim has always challenged me to express my research as clearly as possible and patiently answered my queries on fabrication and microscopy. I am also thankful to Dr. Richard Hobbs and Yujia Yang for many valuable discussions and suggestions about my research.

In addition to Karl, Chung-Soo, Richie and Yujia, I am also indebted to Prof. Dirk Van Dyck for furthering my understanding of electron microscopy and developing an explanation of the electron diffraction data reported in this thesis. I would also like to thank Prof. Van Dyck, Dr. Ricardo Egoavil, Dr. Ivan Lobato, Stijn Van Den Broeck and Prof. Jo Verbeek for hosting me during my visit to the University of Antwerp, and providing me invaluable tips and suggestions on my research. I would also like to appreciate the help and advice of all of my collaborators on the Quantum Electron Microscope project, including but not limited to Prof. Pieter Kruit, Prof. Peter Hommelhoff, Prof. Mark Kasevich, Dr. Thomas Juffman and Brannon Klopfer.

I would like to express my gratitude to Dr. Yong Zhang and Dr. Shiahn Chen from

the MIT Center for Materials Science and Engineering for teaching my how to use the various electron microscopes and ion-beam tools and always being available to help me with experiments.

Additionally, I would like to thank Prof. Cardinale Warde, my academic adviser, for his helpful discussions on my progress as a graduate student. I also thank all my colleagues, labmates, classmates and friends for many stimulating discussions, and for being a constant source of help and happiness.

I thank the Gordon and Betty Moore Foundation for supporting the Quantum Electron Microscope project.

Finally, I am deeply indebted to my family for teaching me the importance of hard work and perseverance, and their unwavering love and support. In work and in life, it has always been my endeavor to walk the path that they showed me.

# Contents

# List of Figures

# Chapter 1

# Introduction to Interferometry

Interferometry is the technique of superposing two or more waves in order to extract information about their relative phases. This information is lost in direct intensity measurements (such as detection on a photo-sensitive screen); the advantage of interferometry is that it converts relative phase variations into amplitude variations which such measurements can record. To illustrate this point, consider two plane waves with amplitudes $E_1$ and $E_2$ and a relative phase difference $\phi$ impinging upon a screen at an angle $\theta$ with respect to each other. The field amplitudes of the two beams can be represented as $A_1 = E_1 e^{i(k_x x + k_y y)} e^{ikz}$ and $A_2 = E_2 e^{i(k_x x - k_y y)} e^{i\phi} e^{ikz}$, with $z$ being the direction of propagation, k the wavenumber and $k_y = \frac{k}{sin\frac{\theta}{2}}$. A direct measurement of the intensities of the two beams would result in $|E_1|^2$ and $|E_2|^2$ respectively and thus we lose information of $\phi$. When the two beams interfere, the intensity is given by:

$$I = \left|E_1 e^{i(k_x x + k_y y)} + E_2 e^{i(k_x x - k_y y)} e^{i\phi}\right|^2 = |E_1|^2 + |E_2|^2 + 2E_1 E_2 cos\left(k_y y + \frac{\phi}{2}\right) \qquad (1.1)$$

Hence by mapping out the sinusoidal variations in the intensity $\phi$ can be measured. Interferometry usually involves four steps [1]:

1. Preparation of the beam in a well-defined initial state (i.e., preparation of a *coherent* beam)

2. Separation of the beam into two or more localized components with a well-defined relative phase

3. Propagation of the components along separate optical paths. In this step the components may experience a relative phase shift due to different path lengths or the presence of an inhomogeneous field.

4. Recombination of the components to convert relative phase differences into intensity modulations

## 1.1 Coherence and its relevance to interferometry

The coherence of the initial beam is critical to the success of any interferometric measurement. Coherence can be quantified through two parameters: *temporal coherence*, related to the spread of frequencies in the beam, and *spatial coherence*, related to the size of the beam source.

### 1.1.1 Temporal coherence

A monochromatic beam of light has a well-defined phase at all points along its propagation. As the spread of frequencies in the beam increases, the phase difference between any two points along the beam becomes ill-defined since the phases contributed by each frequency component vary at different rates. We define the *temporal coherence length* $L_{\mathrm{ct}}$ as the maximum separation between two points along the beam (or the maximum propagation length) over which the phase is well-defined.

$$L_{\mathrm{ct}} = \frac{Kc}{\Delta\nu} \tag{1.2}$$

where $c$ is the speed of light, $\Delta\nu$ the bandwidth, $K$ a constant of order 1 that depends on the exact shape of the beam's frequency spectrum. Temporal coherence is important

with regard to steps 3 and 4 of the interferometric process outlined above. The recombining beams are derived from the same initial beam and have propagated through different optical paths. Such experiments typically use time-integrated intensity measurements, so if the optical path-length difference (OPD) is greater than $L_{ct}$ the interference gets washed out by the fluctuating relative phase difference between the paths. An important criterion for interferometry thus is that the OPD must be smaller than $L_{ct}$.

### 1.1.2 Spatial coherence

Spatial coherence is intimately related to the size of the source that produces the beam. To visualize this relation, I depict in figure 1.1(a) the 2-D circular wavefronts produced by an ideal, monochromatic point source. The radius vector from the source to any point on a wavefront defines the direction of the wave at that point, and is unambiguous. Figure 1.1 (a) shows some examples of the direction of the wave at different points. We can thus define a fixed phase relationship between any two points in the wave, by looking at the wavefronts on which they are located. A real source does not emit continuous waves but wavepackets of finite duration; different wavepackets do not have a definite phase relationship. However, this indefinite phase relationship does not affect the relative phase between two given points as a given wavepacket propagates through them; any overall phase between different wavepackets makes no difference to the relative phase between the two points. If we now add a second ideal point source close to the first one, shown in red in figure 1.1(b), each point now has two radius vectors (point A, for example); one from each source, and hence the direction at each point is not as clear. Further, if the second source does not have a fixed phase relationship with the first one, points such as A and B that are on the same wavefront with respect to the first wave but not the second will not have a well-defined relative phase. Note however that points C and D, which are much closer to each other, are almost on the same wavefront in the same direction for both sources and thus it is easier to define the relative phase between them. An extended source can be treated as a collection of mutually incoherent point sources

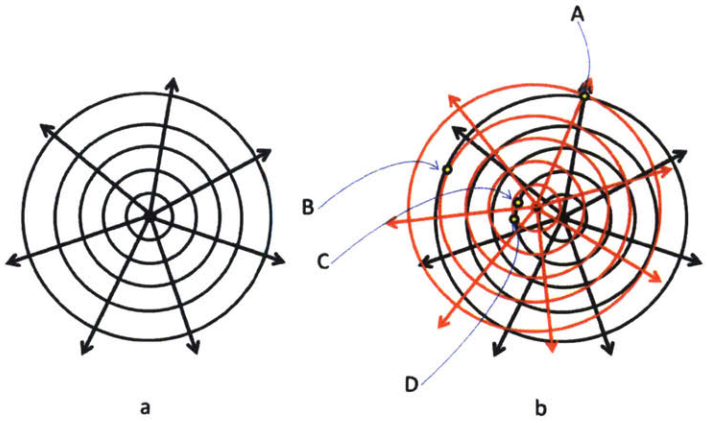


Figure 1.1: Spatial coherence for point and extended sources. (a) An ideal point source produces waves of infinite spatial coherence, meaning that the direction of the wave is well defined at each point on the wavefront. (b) The introduction of another independent point source that does not have a fixed phase relation with the first reduces the spatial coherence by introducing ambiguity in the relative phase between points such as A and B, which are on the same wavefront for one source but not the other. Points C and D, which are close to each other still have a relatively well defined mutual phase. Thus for extended sources the phase along the wavefront is well-defined only up to the *spatial coherence length* $L_{\mathrm{cs}}$.

(*i.e.*, point sources that do not have a fixed relative phase difference) , and thus the waves it produces have a well-defined phase over a limited length known as the *spatial coherence length* $L_{\mathrm{cs}}$. Spatial coherence is again relevant to the recombining beams; if they are derived from points on the original beam separated by a distance greater than $L_{\mathrm{cs}}$, the ill-defined phase washes out interference effects.

### 1.1.3 Fringe contrast and the degree of coherence

Going back to equation 1.1, the *contrast* $C_o$ of the interference fringes, defined as the ratio of the difference and sum of the maximum and minimum intensities:

$$C_o = \frac{I_{\max} - I_{\min}}{I_{\max} + I_{\min}} = \frac{2E_1E_2}{|E_1|^2 + |E_2|^2} \tag{1.3}$$

Assuming the two interfering waves have equal amplitudes, $C_o = 1$. However, as discussed in sections 1.1.1 and 1.1.2, if the waves have limited spatial or temporal coherence, the incoherent 'parts' of the waves do not produce interference fringes since their relative phase difference is not fixed. Averaged over time, this incoherent addition adds a uniform background to the interference pattern which reduces the contrast to $C = \mu C_o$. Here $\mu$ is the *degree of coherence* and can be written as the product of $\mu_{tc}$ and $\mu_{sc}$ which denote the temporal and spatial degrees of coherence respectively. Thus (assuming equal interfering amplitudes), the fringe contrast can be used to measure the degree of coherence of the initial beam and hence characterize step 1 of the interference process outlined earlier.

## 1.2 Young's double-slit experiment

The double-slit experiment, first performed by the English physicist Thomas Young in 1803 unambiguously demonstrated the wave nature of light and is the simplest example of an interferometer. The setup, sketched in figure 1.2, consists of an initial single slit followed by two further slits and a screen placed at a large distance from the slits. Incoherent sunlight is incident on the first slit S1. Assuming the slits to be ideal pinholes, S1 spatially filters out all the incident sunlight except at one point and thus creates an ideal point source emitting coherent, spherical wavefronts. This filtering is step 1 of the interferometry process outlined earlier. We can also use a frequency filter to increase the temporal coherence of the light. The wavefronts from S1 are now incident on the double slit S2, which blocks the wavefronts

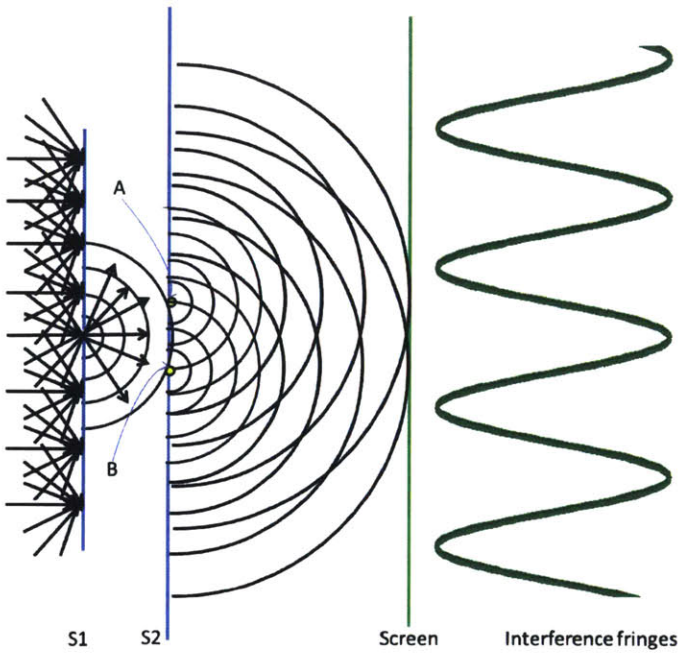


Figure 1.2: Young's double-slit experiment. Initially incoherent light is incident upon the slit S1 which acts as a spatial filter and produces light of greater spatial coherence, which is then incident on the double-slit S2 (slits at A and B). The two slits act as sources of cylindrical waves which overlap and interfere on the screen, leading to sinusoidal fringes.

except at the two pinholes. This is step 2, state separation. Beams from the two slits then propagate to the screen (step 3) where they overlap and interfere, giving rise to intensity modulations (step 4), which manifest as interference fringes on the screen. In a realistic experiment, the diameter of slit S1 controls the degree of spatial coherence of light incident on S2; a larger diameter means a larger source and hence reduced coherence. Modern versions of the double-slit experiment employ a laser as the light source which eliminates the need for S1 since the light produced by the laser source has a high degree of coherence.

## 1.3 Wavefront and amplitude-division interferometry

Young's double-slit experiment is an example of a *wavefront-division interferometer*, since the two localized components (step 2) are derived from two points along the same wavefront of the initial beam. These two points are marked as A and B in figure 1.2. The Fresnel biprism interferometer in which the double-slit is replaced by two stacked prisms to create virtual point sources is another example of a wavefront-division interferometer. Such interferometers require $L_{cs}$ to be greater than the separation between the two points on the wavefront that produce localized waves to ensure that they are coherent. Thus in figure 1.2, $L_{cs}$ of the wave after S1 must be greater than the distance between A and B for high contrast interference fringes.

*Amplitude-division interferometers* produce localization by splitting the amplitude of the incident beam. Examples include the Michelson and Mach-Zehnder interferometers (figure 1.3 (a) and (b) respectively) which employ beamsplitters (labeled 1 in figure 1.3) to divide the amplitude of the incident beam along two paths which may have a relative OPD. Mirrors (2 and 3) redirect the two paths back towards each other and second beamsplitter (for the Mach-Zehnder, labeled 4) or a second incidence on the same beamsplitter (for the Michelson) recombines the two beams leading to interference. The intensities at the output detectors depend upon the OPD between the two paths (blue and green) and can be varied by moving the mirrors or beamsplitters. In figure 1.3, we trace the paths of two initially co-incident points A and B as the beam propagates through the system. We see that the two points coincide again upon recombination in both interferometers. Since neighboring points in the incident beam remain close to each other in the output beam (unlike wavefront-division interferometers), $L_{cs}$ just needs to be greater than a few fringe periods. Therefore, the spatial coherence requirements in amplitude-division interferometry are much more relaxed than in wavefront-division interferometry. However, this relaxation comes at the cost of reduced resolution for low-coherence sources. The resolution in amplitude-division interferometry is limited by the period of the gratings employed. This is not a limitation for wavefront-division

interferometers [2].

## 1.4 Electron interferometry

The field of electron optics began with the demonstration of the wave nature of electrons by the diffraction experiments of Thomson [3], and Davisson and Germer [4] in 1927. Independent of this work, Ernst Ruska and Max Knoll constructed the first electron microscope and soon after beat the best attainable resolution of optical microscopes. The first suggestion for a interferometeric measurement with electrons was made by Dennis Gabor in 1948 [5]. His idea (*inline electron holography*) involved placing an object in the path of a beam of electrons, and mapping phase variations over the object from the interference between the part of the beam that passed through the object and the part that does not.

The first electron interferometer was not developed until 1954, when Marton and coworkers [6, 7, 8] demonstrated an amplitude-division interferometer with a 60 kV electron beam. The interferometer consisted of three 10-nm-thick, crystalline, epitaxially-grown copper membranes which acted as diffraction gratings. These interferometers used diffraction as the mechanism for beamsplitting and recombination. Figure 1.4(a) schematically depicts such a three-grating interferometer. To simplify the description, we use a 1-D grating with lattice constant $a$ and depict only the zeroth and first order diffracted waves from each grating. Solid lines represent the waves that form the interferometer. I use Zhou's notation [9] to depict the various diffracted beams from the two gratings. The first grating splits the incident wave $\Psi$ into the zero ($\Psi_{\mathbf{0}}$, red) and first order diffracted partial waves ($\Psi_{\mathbf{g}}$, orange and $\Psi_{\bar{\mathbf{g}}}$, black). Here $|\mathbf{g}| = 2\pi/a$ is the (1-D) reciprocal lattice vector. Each of these waves is incident at a Bragg angle on the second grating and gets diffracted again, provided the two gratings are mutually aligned. The re-diffracted partial waves arising from $\Psi_{\mathbf{0}}$ are $\Psi_{\mathbf{00}}$ (red), $\Psi_{\mathbf{0g}}$ (green), and $\Psi_{\mathbf{0\bar{g}}}$ (black), and similarly for $\Psi_{\mathbf{g}}$ ($\Psi_{\mathbf{g0}}$, $\Psi_{\mathbf{g\bar{g}}}$ (orange)) and $\Psi_{\bar{\mathbf{g}}}$ ($\Psi_{\bar{\mathbf{g}}\mathbf{0}}$ and $\Psi_{\bar{\mathbf{g}}\mathbf{g}}(black)$, both black). Defining $\mathbf{g}_{\text{net}}$ as the sum of the subscript $\mathbf{g}$-vectors

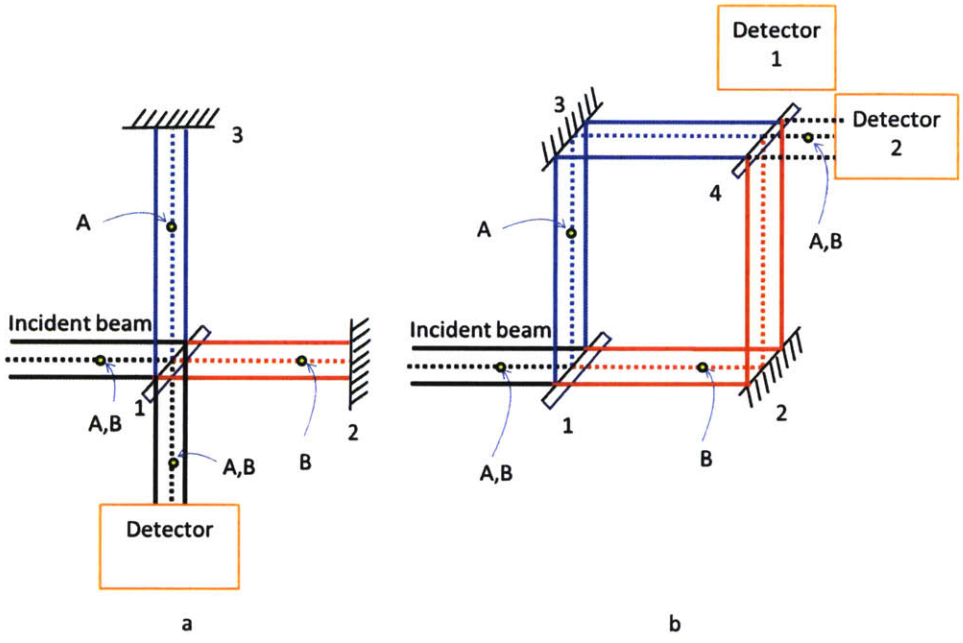


Figure 1.3: Amplitude-division interferometry. (a) Michelson interferometer. Beamsplitter 1 splits the incident beam along the red and blue paths, which reflect from mirrors 2 and 3 and recombine on the beamsplitter. The intensity at the detector depends on the OPD between the two paths and can be changed by moving one of the mirrors. (b) Mach-Zehnder interferometer: beamsplitter 1 creates two beams which are redirected towards each other by mirrors 2 and 3. They recombine on beamsplitter 4 such that there is completely constructive interference towards detector 2 and completely destructive interference towards 1. In both interferometers, points A and B which are initially co-incident and separate out at the first beamsplitter are recombined in the output beam. Thus the coherence between neighboring points of the output beam is governed by the coherence between the same points in the input beam. Therefore. the spatial coherence requirement is lower for amplitude-division interferometers than it is for wavefront-division interferometry.

for each of the waves, we see that any two diffracted waves $\Psi_{\mathbf{g1g2}}$ and $\Psi_{\mathbf{g3g4}}$ for which $|\Delta\mathbf{g}_{\text{net}}| = |(\mathbf{g3}+\mathbf{g4})-(\mathbf{g1}+\mathbf{g2})| = 0$, such as $\Psi_{\bar{\mathbf{g}}\mathbf{g}}$ and $\Psi_{\mathbf{00}}$, or $\Psi_{\mathbf{0g}}$ and $\Psi_{\mathbf{g0}}$ emerge parallel to each other after diffraction from both gratings. Waves with $|\Delta\mathbf{g}_{\text{net}}| = \mathbf{g}$ such as $\Psi_{\mathbf{0g}}$ and $\Psi_{\mathbf{g}\bar{\mathbf{g}}}$ overlap and interfere with each other at a distance $D$ equal to the gap between the first two gratings. We will henceforth refer to this plane as the interference plane. This overlap leads to interference fringes which can be read out by placing a third grating in the overlap plane and recording the electron counts on an integrating detector positioned in the path of either of the output waves. Translation of the third grating perpendicular to the optical axis leads to oscillations in these counts due to change in the relative phase between the two interfering waves. Equivalent interferometers are formed by any two diffracted waves for which $|\Delta\mathbf{g}_{\text{net}}| = \mathbf{g}$, for example, $\Psi_{\bar{\mathbf{g}}\mathbf{g}}$ and $\Psi_{\mathbf{0}\bar{\mathbf{g}}}$. If the paths of the interfering beams are fully separated, the three-grating interferometer can act as a Mach-Zehnder interferometer for electrons.

Despite this demonstration, it was only after the development of the electron biprism by Möllenstedt and Düker in 1956 [10] and the use of a field-emission gun (FEG) in electron microscopy by Crewe and co-workers in 1968[11] that electron interferometry techniques became widespread. The electron biprism, depicted schematically in figure 1.4(b), is a thin positively charged wire that blocks part of the incident electron beam and deflects the resulting partial waves (shown in blue and yellow) towards each other. These waves recombine (green) on a screen, producing interference fringes. The incorporation of the biprism in the transmission electron microscope enabled *off-axis electron holography* [12], where an object is placed in the path of one of the separated partial waves and shifts in the observed interference fringes are used to map phase variations over the object in a manner similar to the example presented in section 1. Being a wavefront-division technique, holography with a biprism requires a highly coherent electron beam (hence the need for a field-emission source [13]). For example, in figure 1.4 (b) we trace the paths of two points in the beam, A and B, which overlap on the screen; $L_{\text{cs}}$ of the electron beam must be greater than the their separation.

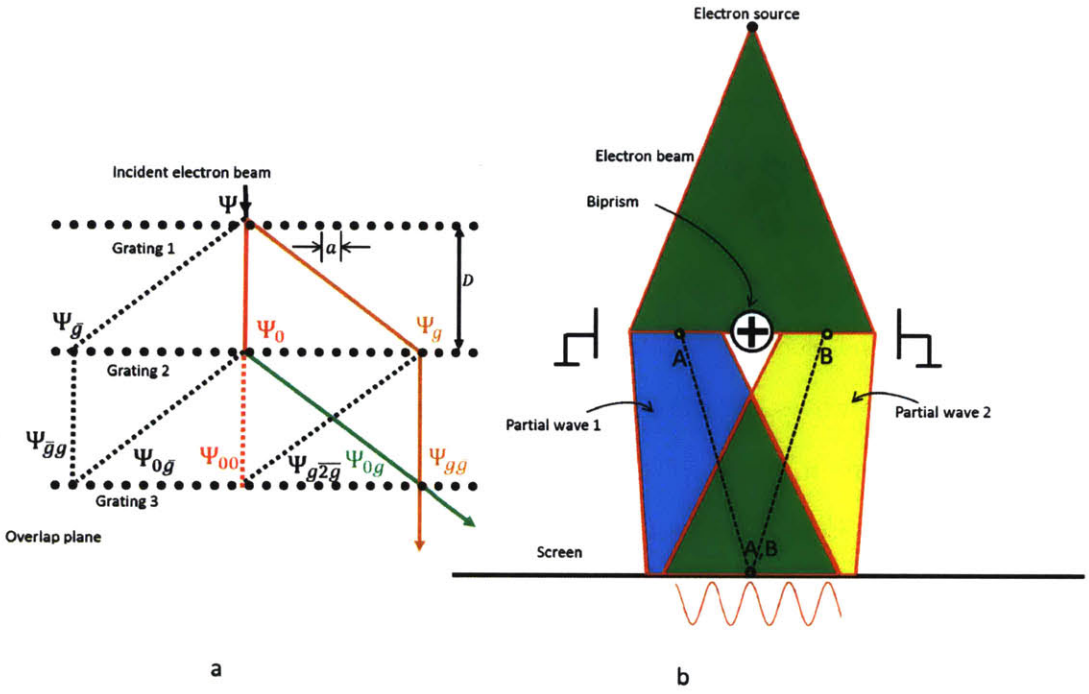


Figure 1.4: Amplitude and wavefront-division electron interferometry. (a) Marton's scheme for a three-grating amplitude-division interferometer. The incident wave $\Psi$ is diffracted into zero ($\Psi_{\mathbf{0}}$) and first ($\Psi_{\mathbf{g}}$ and $\Psi_{\bar{\mathbf{g}}}$) order beams by grating 1, each of which diffracts again from grating 2. Any two diffracted partial waves with $\Delta\mathbf{g}_{\mathrm{net}}$(see text for definition) $= \mathbf{g}$, such as $\Psi_{\mathbf{0g}}$ and $\Psi_{\mathbf{g\bar{g}}}$ interfere in the 'interference plane', thereby imaging the lattice planes corresponding to $\mathbf{g}$ onto this plane. This image can be read out by placing a third grating in this plane, translating it perpendicular to the optical axis and recording the change in intensity along either beam path. (b) Wavefront-division interferometry with an electron biprism. The biprism shadows out part of the incident beam (red) and redirects the resulting partial waves (blue and yellow) towards each other, leading to interference on the screen (green). The intensity at a given point on the screen arises from overlap between two separated points in the initial beam (A and B), and hence $L_{\mathrm{cs}}$ must be large enough to ensure coherence between these points.

The requirement for coherence is met by the FEG. In this gun, electrons are pulled out of a

| Electron gun | source size (nm) |
|---|---|
| Thermionic (Tungsten) | $> 10^5$ |
| Thermionic ($LaB_6$) | $10^4$ |
| Schottky FEG | 15 |
| Cold FEG | 3 |

Table 1.1: Effective electron source size produced by different types of electron guns

sharp metal tip by the application of a very high electric field which reduces the potential barrier at the surface of the metal. The other commonly used method of producing an electron beam involves *thermionic emission* from a tip (tungsten or $LaB_6$). In an FEG, elevated temperatures are not required and hence it is also called a *cold-FEG*. A third type of gun, the *Schottky FEG*, combines characteristics of thermionic and cold-FEG by producing the beam with the application of a high electric field at elevated temperatures. Table 1.1 compares the effective source size produced by these two methods[14]. We see that the cold-FEG produces the smallest source size and hence the most coherent beam. However cold-FEGs are more susceptible to instabilities in electron current than thermionic guns. The Schottky FEG is a good compromise between the stability of the thermionic gun and small source size of the cold-FEG. Aided by FEGs, electron holography has been used in many applications such as exit-wave reconstruction [12], demonstration of the Aharonov-Bohm effect[15] and imaging magnetotactic bacteria [16].

Following Marton's initial experiments, amplitude-division interferometry with mechanical gratings was not widely researched or employed. In the 1970's, Dowell and Goodman obtained interference between electrons diffracted from two overlapping thin crystals [17, 18], and Buxton, Rackham, and co-workers obtained interference from two crystalline layers of silicon separated by 1-2 µm formed by ion-beam milling at the edge of a crystal [19, 20]. This "double-crystal interferometer" was later replicated and studied by Zhou in 1995 [21, 9]. Single crystalline gratings combined with biprisms have also been employed in interferometry and holography setups by Herring [22, 23], Ru [24] and Mertens [25].

Besides crystalline gratings, electron diffraction from nanofabricated gratings (as demonstrated by Jönsson in 1961[26]) has also been used in interferometry. Progress in nanofabrication techniques such as optical lithography, electron beam lithography (EBL), and focused ion-beam milling (FIB) in the last few decades has enabled faster and more accurate fabrication of gratings and other diffractive optics for electrons. Ito et al. used a scanning transmission electron microscope to fabricate 2D diffraction gratings [27] and Fresnel lenses[28]. More recently, Gronniger et al. [29, 30] and Bach et al. [31] constructed Mach-Zehnder and Talbot-Lau electron interferometers using three large gratings fabricated by optical interference lithography. Verbeek et al. [32] and McMorran et al. [33] fabricated phase plates using FIB to create electron vortex beams. Frabboni et al.[34, 35, 36, 37, 38] and Bach et al. [39] demonstrated Feynman's which-way thought experiment in FIB-fabricated double-slit electron interferometers.

The lack of progress in the field of amplitude-division electron interferometry, despite the advances outlined above, is in sharp contrast to atomic and molecular interferometry where both mechanical and optical grating interferometers have been heavily researched and are well-developed [1]. This lack of adoption is primarily due to the stringent requirements of positioning and orientation for precise alignment of the interferometer. In his interferometer, Marton[8] developed mechanical manipulators that could control translation and rotation of each grating accurately. The three gratings were then aligned by taking micrographs of the diffracted beams. This effort required considerable modification of the electron microscope column. Gronniger's experiment[30] used an external laser interferometer for alignment. The double crystal interferometer of Buxton and Zhou overcame the requirement of alignment but had limited applicability due to the small gap between the crystals which made separation of interferometer paths difficult [40].

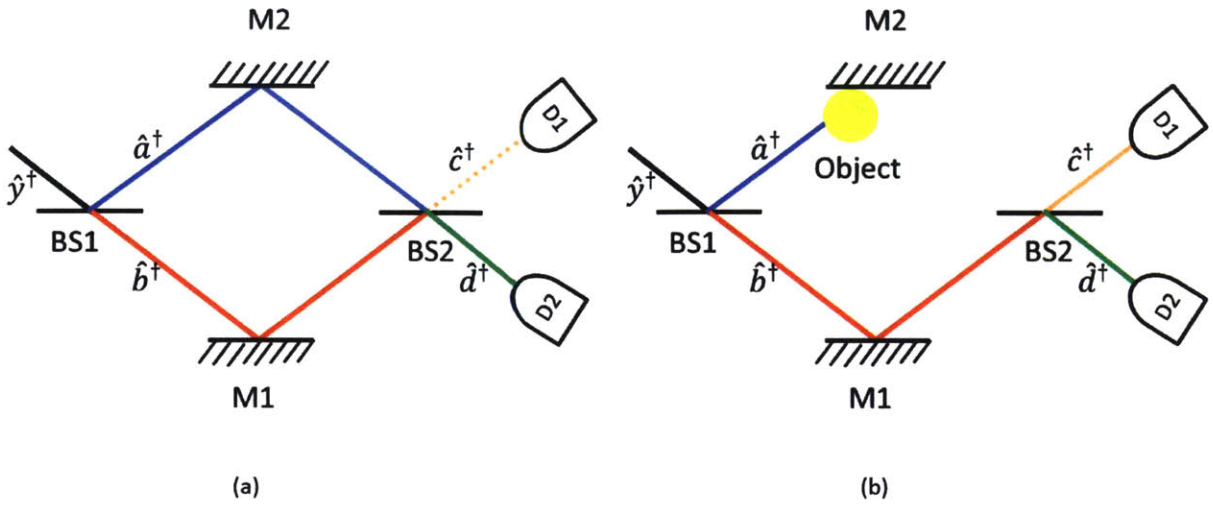


Figure 1.5: Elitzur-Vaidman scheme for a Mach-Zehnder interferometer. (a) Without an object, beamsplitter BS2 the two paths created by BS1 to interfere constructively towards detector D2 and destructively towards D1. Thus an input photon is always registered at D2.$\widehat{y}^\dagger$ is the photon creation operator along the input arm, $\widehat{a}^\dagger$ along the upper arm (blue), $\widehat{b}^\dagger$ along the lower arm (red), $\widehat{c}^\dagger$ along the upper output arm (orange), and $\widehat{d}^\dagger$ along the lower output arm (green). M1 and M2 are mirrors that redirect the paths towards BS2. (b) With an object in the upper arm, the interference is blocked and hence photon counts are registered on both D1 and D2 with probability 0.25. Counts at D1 constitute IFM.

## 1.5 Interaction-free measurements with interferometry

The wave description of interferometry, as outlined above, was sufficient for most classical experiments. However, the formulation of quantum mechanics in the 1920's and 30's resulted in an alternative way of approaching interferometry from the point-of-view of *wave-particle duality*. *Interaction-free measurement* is of the most interesting proposed applications of this approach.

### 1.5.1 The Elitzur-Vaidman bomb-testing thought experiment

In 1993, physicists A. Elitzur and L. Vaidman proposed a thought experiment that used the non-locality of quantum mechanics to infer (in some cases) the presence of a classical, 100 % absorbing object without any photons directly interacting with it[41]. Their 'interaction-free measurement' (IFM) scheme is sketched in figure 1.5. The object being measured is placed in one of the arms of a Mach-Zehnder interferometer. As explained in section 1.3, the Mach-Zehnder interferometer uses a beamsplitter to divide the amplitude of the incoming probing particles into two paths which are then recombined using a pair of mirrors and a second beamsplitter. We denote the photon creation operator along the beam path incident on the first beamsplitter (black in figure 1.5) as $\widehat{y}^\dagger$, along the upper interferometer arm (blue) as $\widehat{a}^\dagger$, the lower arm (red) as $\widehat{b}^\dagger$, the upper output (orange) from the second beamsplitter as $\widehat{c}^\dagger$, and the lower output (green) with $\widehat{d}^\dagger$. Kets $|0\rangle_s$ and $|1\rangle_s$ represent 0 and 1 photon along path $s$ respectively; thus $\widehat{s}^\dagger |0\rangle_s = |1\rangle_s$. For 50 % transmitting beamsplitters, an input photon has equal probabilities of being in either of the interferometer arms. Hence, the creation operator at the input transforms as:

$$\widehat{y}^\dagger \rightarrow \frac{\widehat{a}^\dagger - \widehat{b}^\dagger}{\sqrt{2}} \tag{1.4}$$

Similarly at the second beamsplitter,

$$\widehat{a}^\dagger \rightarrow \frac{\widehat{c}^\dagger + \widehat{d}^\dagger}{\sqrt{2}} \tag{1.5}$$

$$\widehat{b}^\dagger \rightarrow \frac{\widehat{c}^\dagger - \widehat{d}^\dagger}{\sqrt{2}} \tag{1.6}$$

where the change in sign for $\widehat{a}^\dagger$ occurs because reflection along the upper arm leads to a phase change of $\pi$ while reflection along the lower arm does not. For a single photon input

into the interferometer,

$$\widehat{y}^{\dagger}\left|0\right\rangle \rightarrow \frac{\widehat{a}^{\dagger}-\widehat{b}^{\dagger}}{\sqrt{2}}\left|0\right\rangle \rightarrow \frac{1}{\sqrt{2}}\{\frac{\widehat{c}^{\dagger}+\widehat{d}^{\dagger}}{\sqrt{2}}-\frac{\widehat{c}^{\dagger}-\widehat{d}^{\dagger}}{\sqrt{2}}\}\left|0\right\rangle \rightarrow \widehat{d}^{\dagger}\left|0\right\rangle \rightarrow \left|1\right\rangle_{d} \tag{1.7}$$

and thus the photon always exits at the lower output of the interferometer. Physically this phenomenon occurs because of constructive interference in the direction of the lower output and destructive in the direction of the upper output. Detector D2, placed at the lower output in figure 1.5(a) always registers a count for every input photon while detector D1 at the upper output never registers a count. If a 100 % absorbing object is now placed in the upper arm of the interferometer as in figure 1.5(b), a photon that takes the upper arm gets absorbed by the object and thus the interference is broken. Mathematically,

$$\begin{aligned}
\widehat{y}^{\dagger}\left|0\right\rangle &\rightarrow \frac{\widehat{a}^{\dagger}-\widehat{b}^{\dagger}}{\sqrt{2}}\left|0\right\rangle \\
&\rightarrow \frac{\widehat{a}^{\dagger}}{\sqrt{2}}\left|0\right\rangle - \frac{\left|absorption\right\rangle}{\sqrt{2}} \\
&\rightarrow \frac{\widehat{c}^{\dagger}+\widehat{d}^{\dagger}}{2}\left|0\right\rangle - \frac{\left|absorption\right\rangle}{\sqrt{2}} \\
&\rightarrow \frac{\left|1\right\rangle_{c}}{2}+\frac{\left|1\right\rangle_{d}}{2} - \frac{\left|absorption\right\rangle}{\sqrt{2}}
\end{aligned} \tag{1.8}$$

Now an input photon will be counted at detectors D2 and D1 with probability 0.25 for each, and will be absorbed by the object with probability 0.5. Counts at detector D2 do not provide us any new information since this detector would click even in the absence of the object. However counts at detector D1 immediately tell us that the object is present, since this detector cannot register counts in the absence of the object as seen in equation 1.7. Photons registered at detector Y could not have been absorbed by the object however; hence we have inferred the presence of the object without interacting or hitting it with the photon. Photon detection at Y only happens in 25 % of the cases; and 50 % of the photons still hit the object.

An alternative formulation in terms of the measurement process is as follows: in the

experiment without the object we do not measure which arm the photon is in, and as a result it behaves as a wave and shows interference. The presence of an object is equivalent to a measurement (to elucidate this point Elitzur and Vaidman used a bomb that is triggered by a single photon as their object; the explosion of the bomb tells us which arm the photon is in). This measurement destroys the wave-like behavior of the photon, resulting in equal probabilities of detection at either detector.

IFM with photons was first demonstrated in 1998 by Kwiat and co-workers [42], who also proposed a scheme for improving the efficiency of IFM by nesting several Mach-Zehnder interferometers and reducing the beamsplitting ratio[43]. Putnam and Yanik [44] suggested a scheme for implementing high-efficiency IFM with electrons, following which designs for such a 'Quantum Electron Microscope' (QEM) were outlined by Kruit et al. [45]. The most significant advantage of such a microscope would be potentially atomic-resolution imaging of the specimen with beam-induced damage reduced by several orders of magnitude due to the reduced interaction between the specimen and probe beam. Beam-induced damage is a major problem in conventional transmission electron microscopy (TEM) as outlined in the next section.

### 1.5.2 Quantum Electron Microscopy

The TEM is a robust, versatile tool that has been used for several decades to image specimens with atomic-scale resolution [14]. With the advent of aberration-correction techniques the maximum achievable resolution has reduced to as low as 50 pm[46]. The microscope operates by shooting a high energy (50 keV or more) beam of electrons at the specimen and collecting the unscattered, elastically, and inelastically scattered electrons that pass through it. Unscattered and elastically scattered electrons are used to form phase contrast images while the scattered electrons can be used to not only image the specimen (scanning transmission electron microscopy (STEM) mode imaging) but also study its crystal structure and chemical composition.

An inherent disadvantage of the TEM is damage to the specimen from the highly energetic incident electron beam. This damage is tolerable for inorganic and non-biological samples but has been a major problem in the application of TEM in imaging biological samples for which this radiation dose is often lethal [47]. Grubb and Keller estimated in 1972 that the irradiation received by the specimen during a single recording of a TEM image is equivalent to a 10 megaton hydrogen bomb exploding at a distance of 30 meters away. This heavy dose limits the maximum dose on the sample to $\sim$ 10 electrons per Å$^2$, which increases the signal-to-noise-ratio in high-resolution microscopy and prevents atomic-scale imaging of structures within live biological samples.

Most biological imaging currently utilizes optical microscopy, where the conventional resolution limit is given by Abbe's criterion and is about 200 nm for visible light. Although several techniques have been proposed in recent years to overcome this limit, the best achievable resolution is still in the range of tens of nanometers. For true atomic resolution biological imaging, therefore, an electron beam imaging modality is essential. Recently cryogenic electron microscopy (cryo-EM) [48] has generated a lot of excitement with nearly 0.3 nm resolution images of biological samples [49]; however the technique depends on acquiring images of an ensemble of biological nanoparticles and extracting the structure from these images and is hence susceptible to ensemble inhomogeneity. Besides, the requirement of cryogenic temperatures precludes any possibility of imaging nanostructures within a live cell.

The QEM was thus proposed by Putnam and Yanik [44] as a method of single particle imaging with the potential to substantially reduce specimen damage as compared to a conventional TEM without compromising on resolution.

As a first step towards the QEM, we are working towards demonstrating IFM with electrons by constructing a Mach-Zehnder interferometer in a regular TEM using Marton's three-grating design. In this work, I fabricated a self-aligned electron interferometer using FIB sculpting of a thick single crystal and demonstrate a Mach-Zehnder electron interfer-

ometer by directly imaging the interference between two electron beams diffracted from the gratings in a transmission electron microscope (TEM). The interferometer was integrated in the (TEM) with no modification of the electron column or optics. Diffraction and interference experiments in the TEM confirmed that the grating architecture is well-aligned. This interferometer design is configurable and scalable to larger dimensions and opens up the possibility of electron interferometry and holography in a conventional transmission electron microscope (TEM) with no modification of the optical column or sample holder, in addition to its potential use to demonstrate IFM with electrons.

# Chapter 2

# Nanofabrication of interferometers through focused ion-beam milling

Focused ion beam (FIB) milling is a widely used nanofabrication technique in which a high-energy (generally between 10-50 kV) focused beam of ions is used to knock out atoms from a given substrate to leave behind the desired structure. It is thus a subtractive fabrication process, and FIB tools are often complemented with gas-injection systems (GIS) to allow additive deposition of platinum, carbon etc. FIB allows the preparation of very thin (<50 nm) samples with sub-10 nm control over the thickness. Modern 'dual-beam' systems are equipped with both ion- and electron-beam columns and allow simultaneous fabrication and scanning microscopy with electrons and ions. The most common use of FIB milling is in the preparation of thin cross-sectional samples of nanostructures for transmission electron microscopy.

## 2.1 Fabrication process

The fabrication process described in this section was developed by Dr. Chung-Soo Kim (MIT) and Stijn Van Den Broeck (University of Antwerp). We exploited the precise control over thickness and placement of thin structures offered by FIB (on the FEI Helios Nanolab

600 and 650 dual-beam systems) to fabricate our two-and three-grating interferometers from one monolithic silicon crystal. The silicon crystal was part of a conventional TEM grid called Nanomesh, from Hitachi High-Tech. It has five cantilevers having two thicknesses of 5 and 40 µm (Figure 2.1 (a) and inset).

Figure 2.1 summarizes the steps in our fabrication process. The cantilever was initially placed perpendicular to the ion-beam optical axis. The first step of the fabrication was milling of windows through the 5/40 µm thick silicon cantilevers using 30 kV gallium ion beam (Figure 2.1(b)). These through holes defined the lateral extent of the gratings, and also reduced re-deposition of sputtered silicon in the subsequent milling steps. The cantilever was then placed along the direction of the optical axis and deposited two 3 µm thick platinum layers to define the gratings and further protect them from ion-beam damage (Figure 2.1(c)). Next the unprotected silicon was milled at 30 kV and 21 nA beam current (Figure 2.1(d)). This step at large current and energy milled most of the silicon between the gratings. It was important here to leave substantial ($\sim$ 500 nm) thickness at each grating to allow for some beam focusing errors and resulting damage in the non-milled area. The gratings were then polished, first at successively lower currents (down to 50 pA) and then at lower energies (down to 2 kV) to give the final structure (Figure 2.1(e)). The polishing step thinned down the gratings to $<$ 40 nm and removed most of the amorphous layer formed from ion-beam damage. The final polishing was done at a slight tilt (up to 5° in either direction) to improve the uniformity of thickness each layer. This non-uniformity can be understood from figure 2. When the substrate was perpendicular to the focused beam (Figure 2.2(a)), some sidewall slope was unavoidable due to the convergence of the beam (Figure 2.2(b)). By tilting the sample as in figure 2.2(c), this slope was reduced (figure 2.2(d)). The lateral dimensions of each grating were restricted to 10 µm by 10 µm laterally. A larger area could have caused the final thin membranes to bend.

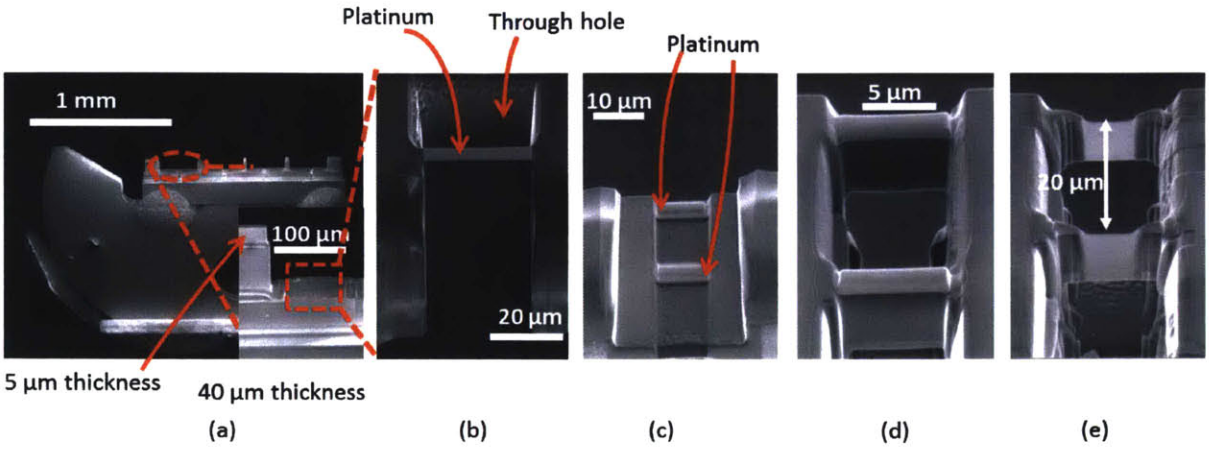


Figure 2.1: Gallium focused-ion beam fabrication of the two-grating structure. (a) Single-crystal silicon TEM grid with cantilevers. Inset is a zoom of the area circled in red with the regions of thickness 5 and 40 µm indicated. (b) Zoom of the 40 µm thickness region showing top layer of deposited platinum over the desired grating region and milled through hole. The through hole reduced re-deposition of milled silicon in subsequent steps and the platinum protected the grating region from damage. (c) Platinum deposited to define the two gratings and protect the underlying silicon from beam damage. (d) The silicon between the two platinum deposits was milled out at high ion-beam energy (30 kV) and current (21 nA) to leave the two unpolished grating regions. The gratings were left thick (500 nm) to prevent the high energy ion-beam from substantially damaging them.(e) Finished gratings after polishing with low current and energy beams. The separation between the gratings for this structure was 20 µm. The thinnest region shows the highest contrast and was kept small to prevent it from bending; it measured ~10 µm in both lateral directions.

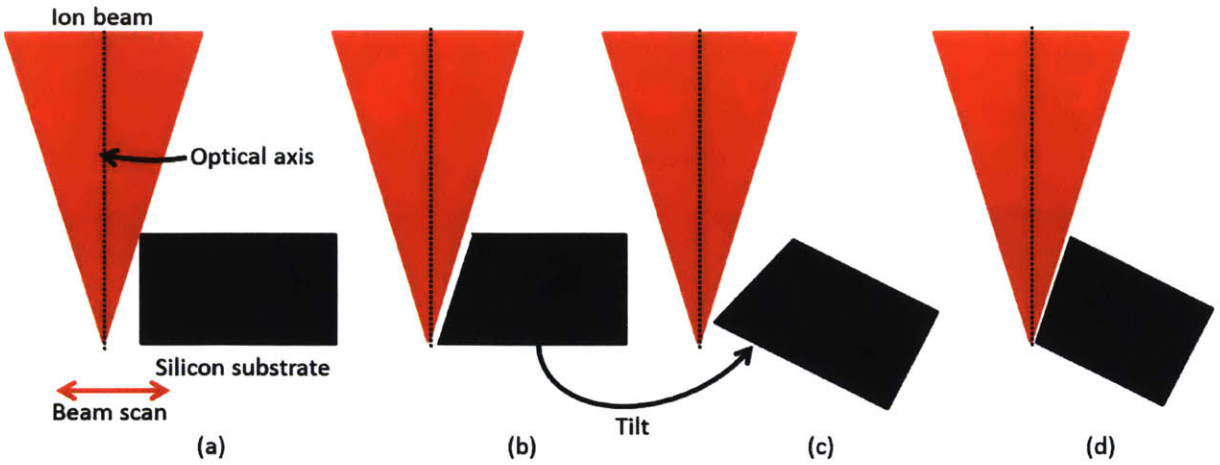


Figure 2.2: The effect of sample tilt on flatness of fabricated structure. (a)-(b) When the sample is perpendicular to the ion beam optical axis, the convergence of the beam leads to slanting sidewalls.(c)-(d) The slant can be reduced by tilting the sample by a few degrees.

## 2.2 Characteristics of the gratings

The fabrication process outlined in the previous section allowed for great flexibility in the spacing and thickness of each grating; figure 2.3 shows some examples of different fabricated geometries. Despite the tilt-assisted polishing step some non-uniformities in the thickness of each grating remained as can be seen from the variation in contrast over each of the gratings in figure 2.3 (b); these non-uniformities are estimated to be on the order of 10 nm. For the three-grating structure the error in the gap between first and second and second and third gratings was $\sim$100 nm; this accuracy will be important later while describing the design of the beam parameters for the interferometer. Figure 2.4 shows a small amorphous region of thickness 13 nm at the edge of one of the gratings which resulted from beam-induced damage. Beyond these amorphous regions the crystalline structure is indicated by the lattice fringes in Figure 2.4.

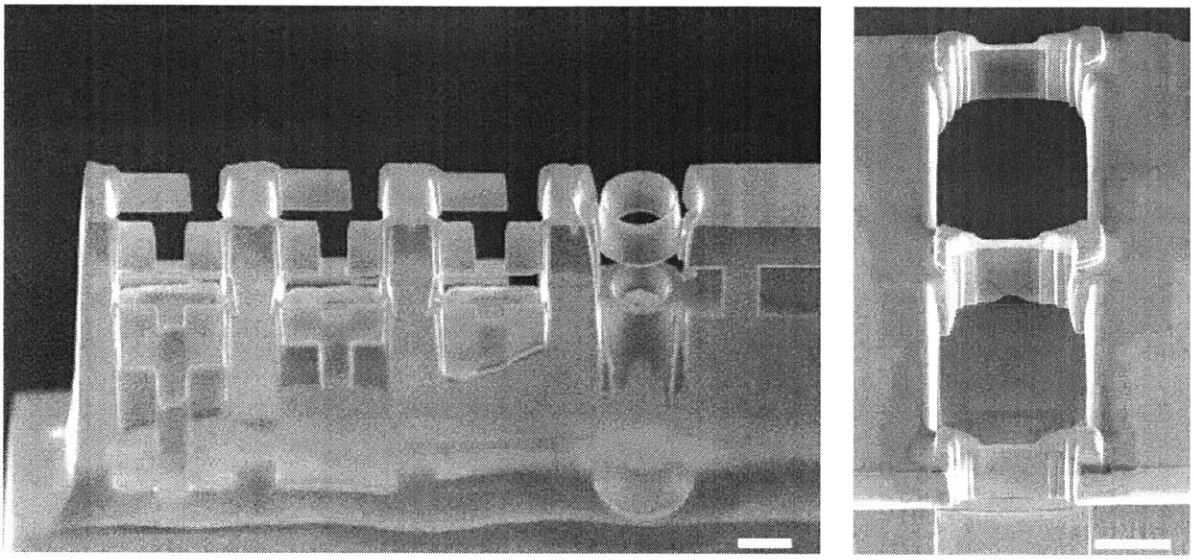


Figure 2.3: Different structures fabricated by FIB. (a) Several two-grating structures with varying geometries, including a cylindrical grating. (b) Three-grating structure. The variation in contrast over each grating is evidence for non-uniform thickness.

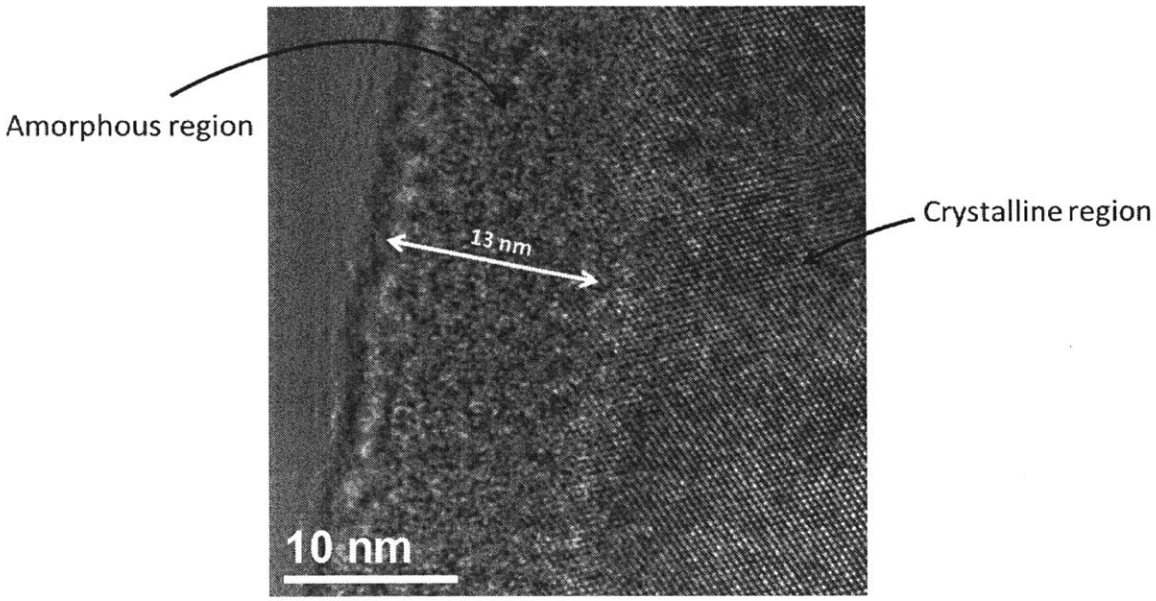


Figure 2.4: Edge of the gratings. A thin layer of amorphous silicon resulted from ion-beam induced damage. Beyond this layer the lattice of crystalline silicon was visible, indicating high crystal quality.

# Chapter 3

# Electron diffraction from two-grating structures

Successful demonstration of interference critically depends on the alignment between the two gratings. Further, the diffracted beams from each grating must retain sufficient coherence to form fringes with good visibility upon interference. Therefore, before performing electron interferometry experiments I checked the alignment of our two-grating structures and the coherence of the diffracted beams by using parallel and convergent electron diffraction through a two-grating structure with 2.5 µm-gap between the gratings.

## 3.1 Grating alignment: parallel beam diffraction

The alignment of the gratings was tested by taking a selected area diffraction pattern (SADP) with a wide, nearly parallel electron beam (semi-angle of convergence $\alpha$ =0.2 mrad) in a JEOL 2010F 200 kV TEM. Figure 3.1(a) shows a ray diagram for parallel beam electron diffraction through the 2.5 µm sample. After diffraction from the two gratings, waves a common value of $\mathbf{g}_{\text{net}}$, *i.e.*, with $\Delta\mathbf{g}_{\text{net}} = 0$ are parallel to each other. Therefore, these waves are focused at the same point in the back focal plane (BFP) of the TEM objective lens. Hence, the focused SADP is expected to be the same as for single-layer silicon, provided the

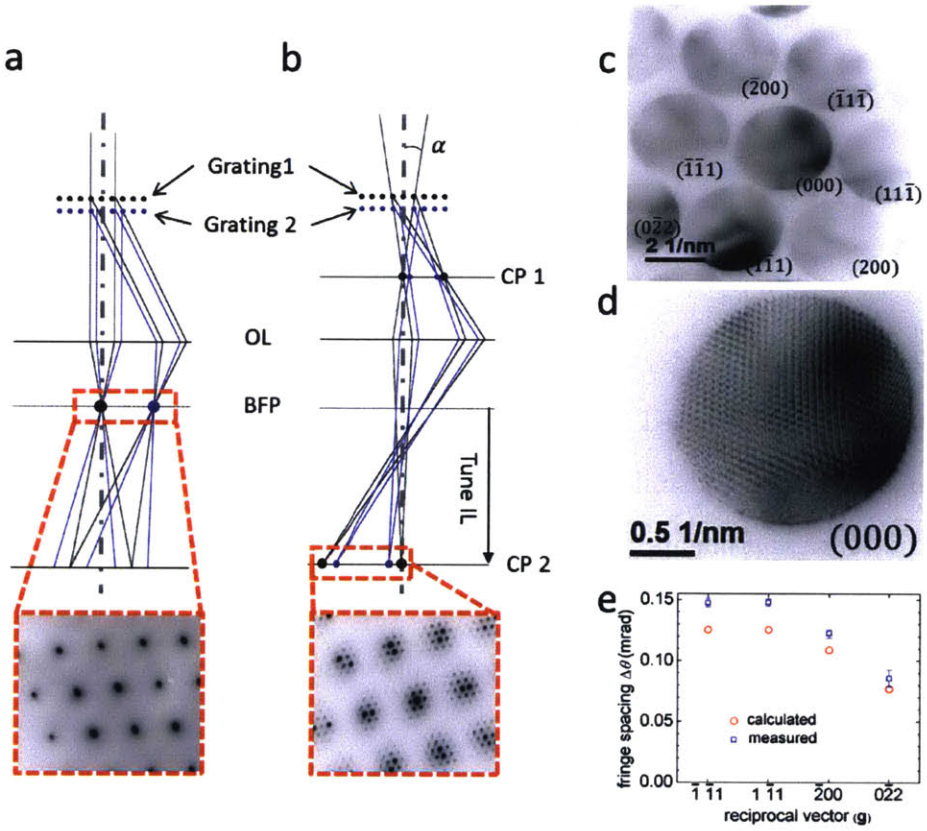
a
b
c
d
e
Grating1
Grating 2
α
CP 1
OL
BFP
Tune IL
CP 2
(200)
(11̄1̄)
(1̄11)
(000)
(11̄1)
(022)
2 1/nm
(200)
0.5 1/nm
(000)
fringe spacing Δθ (mrad)
0.15
0.10
0.05
0.00
calculated
measured
1 11
1 11
200
022
reciprocal vector (g)

Figure 3.1 *(previous page)*: Parallel and convergent-beam diffraction from the two-grating structure.(a) Ray diagram for a nearly parallel incident beam (small $\alpha$). Diffracted beams with $\Delta\mathbf{g}_{\text{net}}$(see text for explanation) = 0 are focused to the same point in the back-focal plane (BFP) of the objective lens (OL). Thus the diffraction pattern is the same as single-layer silicon as seen in the experimentally obtained SADP (red box). The experimental SADP is for $\alpha = 0.1$ mrad. (b) Ray diagram for a convergent incident beam (large $\alpha$). The spots in the BFP broaden to disks formed by overlap between waves with $\Delta\mathbf{g}_{\text{net}} = 0$ which leads to interference fringes within each spot. At the first and second crossover plane (CP 1 and CP 2 respectively), these beams focus at horizontally displaced points due to the gap between the gratings. The red box is the experimental diffraction pattern in the second CP with $\alpha$=10 mrad, showing multiple closely spaced spots due to this horizontal displacement. (c) BFP diffraction pattern with $\alpha$=10 mrad showing interference fringes for the 2.5 µm-gap sample. The $\mathbf{g}_{\text{net}}$ corresponding to each spot is indicated. (d) Magnified view of the $\mathbf{g}_{\text{net}} = (1\bar{1}1)$ spot showing interference fringes (e) Angular separation of fringes in the (000) spot, *i.e.*, formed by interference between diffraction orders with $\mathbf{g}_{\text{net}} = 0$. In this case, the **g**-vectors from the two gratings must be equal in magnitude and oppositely directed. These vectors are indicated on the $x$-axis.

two gratings are well-aligned. This expectation is confirmed in the experimentally observed SADP in the red box in figure 3.1(a). I did not observe any displacement between the focused diffraction spots from the two gratings for camera lengths up to 200 cm.

## 3.2 Coherence: Convergent beam diffraction

Coherence between beams diffracted from the two gratings was tested by increasing $\alpha$ to 4 mrad, a situation depicted schematically in figure 3.1(b). Here I call the plane where the beam is focused the 'first crossover plane' (CP1). Since the diffracted beams from both the layers had the same angular spread, they were also focused in this plane. To obtain the sharpest focus, I needed to tune the intermediate lens current to move below the BFP to the 'second crossover plane' CP2, which was an image of the focused beams at CP1 below the two gratings. In this plane, the gap between the two gratings led to horizontal displacement between the focused spots from beams with the same value of $\mathbf{g}_{\text{net}}$. Note that only two beams are included in Figure 3.1(b) to simplify the discussion; taking all possible orders of diffraction into account (*i.e.*, all allowed $\mathbf{g}_{\text{net}}$) resulted in several closely spaced spots(due to diffraction from the second grating) around each spot from the first grating, as seen in the experimental DP from figure 3.1(b), for $\alpha$ =10 mrad [50]. This diffraction pattern is reminiscent of the Moiré effect, except that the difference in magnification between the layers was created not due to different lattice constants but the gap between the gratings.To verify this explanation of the observed diffraction pattern I performed the following experiments:

1. I first verified that there was significant horizontal displacement of diffracted beams for a single layer of silicon with a convergent beam by fabricating a single silicon grating sample and recording the diffraction pattern from it at different stage heights in the TEM. The reciprocal-space distance between the $\Psi_0$ and first order $\Psi_g$ spots was a measure of this displacement. As can be seen from figure 3.2 (a) this distance changed considerably with stage height. This change in distance did not occur with a parallel

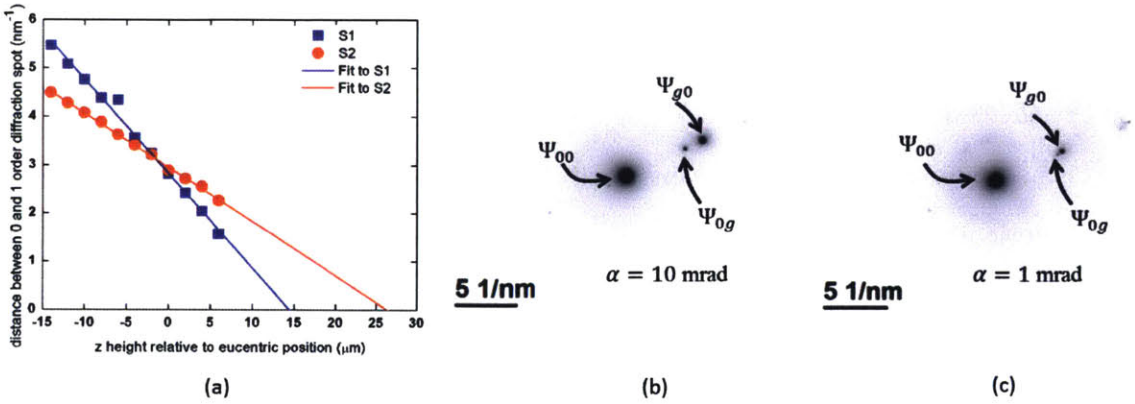


Figure 3.2: Verification of the mechanism of convergent beam diffraction. (a) Variation of distance between $\Psi_0$ and $\Psi_g$ spots at the second crossover plane with variation in stage height for a single-grating sample, for two convergence angles. The change in distance indicates that the origin of horizontal displacement between diffracted beams at the crossover plane is the convergence of the beam. (b) Diffraction pattern at the second crossover plane for two gratings in the two-beam condition, for beam convergence angle $\alpha = 10 and 1$ mrad. The separation between the two spots $\Psi_{g0}$ and $\Psi_{0g}$ with $g = (0\bar{2}2)$ reduces with decreasing convergence angle.

beam, confirming that its source was the convergence of the beam.

2. I next placed the two-gratings in the two-beam condition by appropriately tilting the TEM sample holder, so that I could study just one set of beams $\mathbf{\Psi_{g0}}$ and $\mathbf{\Psi_{0g}}$ ($\mathbf{g} = (0\bar{2}2)$) in figure 3.2) (b) and (c). I then varied the beam convergence angle (by changing the beam spot size), and recorded the diffraction pattern (DP) at the second crossover plane. Figure 3.2 shows the recorded DP for $\alpha = 10$ and 1 mrad. As can be seen, the two spots $\mathbf{\Psi_{g0}}$ and $\mathbf{\Psi_{0g}}$ are closer to each other for a smaller convergence angle(i.e., a more parallel beam).

### 3.2.1 Back-focal plane fringes

As a result of the beam convergence the focused spots in the BFP broadened into disks, with each disk formed by overlap between beams with $\Delta\mathbf{g}_{\text{net}} = 0$. I observed interference fringes with multiple orientations and periods within each of the spots in the BFP, as seen in the SADP in figure 3.1(c). I will henceforth refer to these fringes as 'BFP fringes' to differentiate them from the imaging plane fringes obtained with the 20 µm interferometer. Interference between $\Psi_{\mathbf{00}}$, $\Psi_{\mathbf{g\bar{g}}}$ and $\Psi_{\mathbf{\bar{g}g}}$ led to BFP fringes within the zero-order spot (since $\mathbf{g}_{\text{net}} = 0$ for each of these beams) perpendicular to $\mathbf{g}$, as seen in figure 3.1(d). Similarly interference between $\Psi_{\mathbf{0\bar{g}}}$ and $\Psi_{\mathbf{g2\bar{g}}}$ resulted in BFP fringes in the $\mathbf{g}_{\text{net}} = \bar{\mathbf{g}}$ spot. Inclusion of all the silicon reciprocal lattice vectors in the description would lead to the different interference fringe orientations and periods in Figure 3.1(c) and (d). These BFP fringes confirmed that the beams diffracted from the first and second gratings were at least partially coherent with each other. In previous work by Buxton and Zhou the angular separation between these fringes was estimated to be $\Delta\theta \sim a/D$ [19, 21, 9]. Physically, a larger reciprocal lattice vector and/or gap between the gratings increases the angle of intersection between the overlapping beams in the BFP, thus reducing the period of the resulting fringes. Importantly, Buxton and Zhou's estimate for $\Delta\theta$ does not depend on $\alpha$. I measured $\Delta\theta$ for $\alpha = 4, 2, 0.9$, and 0.5 mrad, by varying the size of the selected-area diffraction (SAD) aperture, keeping all lens currents constant. In figure 3.1(e) I compare the mean of the $\Delta\theta$ for these values of $\alpha$ with Buxton and Zhou's estimate, for fringes within the zero order spot with $\mathbf{g} = (\bar{1}\bar{1}1)$, $(1\bar{1}1)$, $(\bar{2}00)$ and $(0\bar{2}2)$. The experimental values agreed with the estimate to an accuracy of 5%, 9.6%, 5.7% and 3.7% for the four value of $\mathbf{g}$ respectively. The variation in the difference between the experimental values and the estimate was due to residual astigmatism in the objective lens. The change in $\Delta\theta$ with $\alpha$ was smaller than 3% of the mean value, and thus the chief source of error was the pixel size of our CCD detector. The error bars for each value of $\mathbf{g}$ indicate the variation of $\Delta\theta$ with an error of one pixel. Further, the contrast of the BFP fringes increased from 15% (for $\alpha = 4$ mrad) to 33% (for $\alpha = 0.5$ mrad). Since

the temporal coherence length of a Schottky source at 200 keV is several meters, the degree of temporal coherence is close to 1. Hence, the fringe contrast can be used to estimate the degree of spatial coherence of the diffracted beams[12] for different SAD apertures.

### 3.2.2 Results with 20 µm-gap-structure

As described in Chapter 4, I used a 20 µm-gap-structure for electron interferometry experiments. With this gap the BFP fringe period is expected to be $\sim$ 10 times smaller which is very close the resolution limit the CCD detector of our TEM. Thus, I was unable to resolve the BFP fringes with the 20 µm-gap-structure. However, as depicted in figure 3.3, the focused diffraction patterns with parallel (figure 3.3(a)) convergent (figure 3.3 (b)) beams shows the same structure as the 2.5 µm-gap-structure. During the interference experiments reported in chapter 4, I noted a slight displacement between the focused spots from each wave, from which I estimated a misalignment of $\sim$ 100 µrad between the two gratings. Possible causes for this misalignment will be discussed in Chapter 4. However, note that this misalignment was an order of magnitude lower than both the maximum tolerance for Marton's interferometer (1.2 mrad) [8, 51] and the misalignment for Gronniger's interferometer (1 mrad) [30]. Also, as noted earlier, I was able to position each grating with an accuracy of $\Delta D = 100$ nm. Thus the fractional error in positioning of the gratings $\Delta D/D = 0.005$ was greater than Marton's tolerance specifications ($\Delta D/D = 0.004$) and a factor of $\sim$ 6 larger than the corresponding value for Gronniger. More careful fabrication should allow more accurate positioning of the gratings.

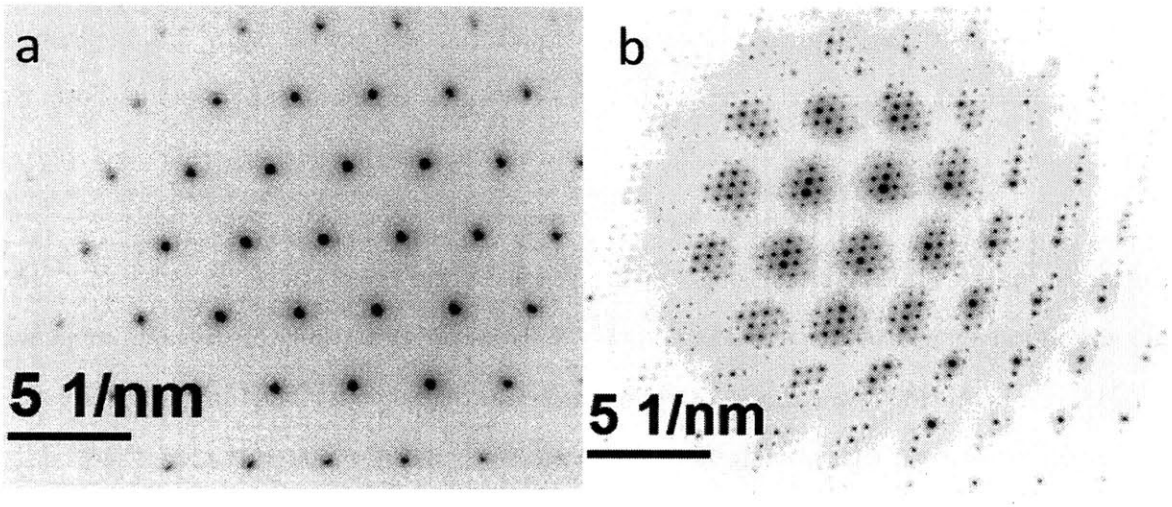


Figure 3.3: Electron diffraction through 20 µm-gap-structure. (a)Parallel beam diffraction pattern, showing alignment of the two gratings. (b) Convergent beam diffraction pattern, showing multiple closely-spaced spots as for the 2.5 µm-gap-structure.

# Chapter 4

# Mach-Zehnder Electron Interferometry

In this chapter I will outline the process of designing the electron interferometer in the Mach-Zehnder geometry and its experimental implementation.

## 4.1 Interferometer Design

The chief goal while designing the interferometer was to ensure complete path-separation of the two diffracted beams. This was found to be unfeasible with the 2.5 µm-gap-structure described in Chapter 3. Using electron diffraction simulations it was determined that a 20 µm-gap was suitable for beam separation.

### 4.1.1 Difficulty of path-separation with small gap between gratings

As demonstrated in the last chapter, the objective lens can be used to obtain interference between beams diffracted from the first and second grating with the 2.5 µm-gap-structure. However, the small gap made it difficult to obtain path separation between the beams. For

200 kV electrons ($\lambda = 2.5$ pm) the distance between the axes of the $\Psi_\mathbf{0}$ and $\Psi_\mathbf{g}$ beams with $\mathbf{g}=(\bar{1}\bar{1}1)$ is just 20 nm on the second grating. One way to obtain path separation is to use a highly convergent beam so that it is focused between the two gratings. However, the use of a highly convergent beam would lead to overlap between the primary and interfering beams (red and intersecting green-orange beams in figure 1.4(a)) in the plane of the third grating and make interpretation of results difficult.

### 4.1.2 Gaussian-Schell model simulations

To determine the optimal set of parameters (beam diameter, convergence angle and grating separation) I simulated the diffraction of 200 kV electrons from two gratings using the Gaussian-Schell model (GSM) [52, 53, 54]. GSM assumes that the incident beam consists of a distribution of independent Gaussian modes and allows for the description of partially coherent beams using the mathematics of Gaussian beams. I used McMorran and Cronin's results on the diffraction of a GSM beam from two gratings[54], with a beam spatial coherence length equal to 20% of the beam diameter in our simulations. This estimate was based on theoretical calculations for small condenser apertures [55, 56], and supported by the preliminary experiments to characterize the beam coherence described in Chapter 3. I used a slightly higher value of the degree of spatial coherence (20%) than that measured in Chapter 4 (15%) for $\alpha = 4$ mrad (which, as I will describe in the following paragraph, was the convergence semi-angle used in the simulations), because of contrast reduction due to unequal amplitudes of the interfering beams. I used the (000) and $(\bar{1}\bar{1}1)$ diffracted beams of silicon to design the interferometer. Therefore, each grating in the simulation was one-dimensional a period of 0.32 nm, which is equal to the period of the $[\bar{1}\bar{1}1]$ lattice planes. An important *caveat* here is that the gratings in my simulation were amplitude gratings, while thin layers of silicon behave as phase gratings at the electron energies used in the TEM. However, this difference did not affect the diffraction angles and hence the set of parameters that allowed the beams to separate, which was the primary focus of the simulations.

With a beam diameter of 200-400 nm, the simulations resulted in a minimum gap of 12-25 µm required between the gratings, to avoid undesirable beam overlap on the second grating and the interference plane. I chose a gap of 20 µm, beam diameter of 240 nm at the first grating, and $\alpha = 4$ mrad, with beam crossover between the second grating and overlap plane. With these parameters the beam diameter in the plane of the second grating and the interference plane was 80 nm. Potentially, I could have used a narrower beam with a smaller $\alpha$ to make beam separation easier. To determine the optimal beam diameter for simulations, I performed preliminary experiments with beam diameters ranging from 60-300 nm and $\alpha$ between 0.5 and 5 mrad. On the JEOL 2010F, beam diameters between 60-200 nm with $\alpha$ less than 4 mrad required the use of a very small (10 µm) condenser aperture which severely limited the intensity of the beams. The reduced beam intensity increased the exposure time required to record interference fringes. The increased exposure time resulted in poor fringe contrast due to stage vibrations. Thus, to obtain good fringe contrast I chose a relatively large beam diameter of 240 nm and $\alpha = 4$ mrad.

Figure 4.1(a) shows the simulated diffraction of a GSM beam with these parameters from two gratings separated by 20 µm. The simulation included diffracted beams up to second order. For all the following simulation and experimental results, $\mathbf{g}=(\bar{1}\bar{1}1)$. As described earlier, any two diffracted beams with $|\Delta\mathbf{g}_{\text{net}}| = \mathbf{g}$ overlap in the interference plane, which for my interferometer was 20 µm below the second grating. In figure 4.1(b), I magnify the region around the interference plane to see the overlapping beams. Note that the fringe contrast in this image was caused by undersampling and consequent aliasing of the underlying lattice-spaced interference pattern in the simulation. However, the extent of these aliased fringes along the optical axis $\Delta z \sim 2.7$ µm was the same as that of the actual interference fringes. $\Delta z$ is proportional to the spatial coherence of the beams, as discussed later. Figure 4.1(c) shows a cross-section of the overlapping beams in the interference plane with further magnification and finer meshing; fringes with the period of the corresponding lattice, *i.e.*, 0.32 nm were now obtained.

Note that there is also overlap between beams with $|\Delta \mathbf{g}_{\text{net}}| = 2\mathbf{g}$, such as $\Psi_{\mathbf{02g}}$ and $\Psi_{\mathbf{g\bar{g}}}$, midway between the second grating and the interference plane. However, the fringes formed from this interference will have half the period of the corresponding lattice. For $\mathbf{g}=(\bar{1}\bar{1}1)$ this period is equal to 0.16 nm which is very close to the resolution limit of the JEOL 2010F. Therefore, I focus only on fringes in the interference plane.

## 4.2 Experimental implementation

I fabricated a 20 µm-gap-structure (figure 2.1(e)) and loaded it into the sample stage of the TEM. Working in a TEM allowed me to directly observe interference fringes between the two diffracted beams by imaging the interference plane; this precluded the need of a third grating to read out interference as described in Chapter 1.

In Figure 4.1(d) I show experimental demonstration of this interferometer geometry. Note that to obtain the electron beam images in this figure, I focused the beams very close to the image plane to make the movement of various beams easier to follow. However, to get high-resolution lattice/interference fringe images, I defocused the beams to the designed diameter and convergence angle. At the TEM stage height $z_1 = 0\,\mu\text{m}$, the second (lower) grating was in the eucentric plane; I imaged the primary and first order diffracted beams ($\Psi_{\mathbf{0}}$ and $\Psi_{\mathbf{g}}$, circled in pink and light green, respectively), on the second grating. The separation $s$ between $\Psi_{\mathbf{0}}$ and $\Psi_{\mathbf{g}}$ was 160 nm as expected for $D = 20\,\mu\text{m}$ ($s = 2\theta_B D$ where $2\theta_B \simeq \lambda_{\text{electron}}/a$). As seen in figure 4.1(e), upon underfocusing the beams to the designed beam diameter (80 nm) at the second grating and imaging $\Psi_{\mathbf{0}}$ at high-resolution, I obtained a lattice-resolved image.

In order to see the various diffracted beams from the second grating, I translated the interferometer vertically by changing the stage $z$ height. This translation enabled me to successively image planes below the second grating. $z_2 = 2\,\mu\text{m}$ below the second grating, I imaged $\Psi_{\mathbf{0g}}$ (circled in blue) at a distance of 15 nm from $\Psi_{\mathbf{00}}$. $\Psi_{\mathbf{g\bar{g}}}$ (circled in dark green)

remained at a distance of 160 nm from $\Psi_{\mathbf{00}}$. I then translated the grating to $z_3 = 5.5\,\mu$m below the second grating. At this plane, the distance between $\Psi_{\mathbf{0g}}$ and $\Psi_{\mathbf{00}}$ increased to 42 nm. $\Psi_{\mathbf{g2\bar{g}}}$ (not circled) was also visible between $\Psi_{\mathbf{0g}}$ and $\Psi_{\mathbf{g\bar{g}}}$. On moving $z_4 = 10.5$ and $z_5 = 16\,\mu$m below the second grating, I observed that $\Psi_{\mathbf{0g}}$ continued moving away from $\Psi_{\mathbf{00}}$ and towards $\Psi_{\mathbf{g\bar{g}}}$. The distance between $\Psi_{\mathbf{0g}}$ and $\Psi_{\mathbf{g\bar{g}}}$ was 78 and 29 nm for $z_4$ and $z_5$ respectively. Finally, when I reached $z_6 = 20\,\mu$m below the second grating, $\Psi_{\mathbf{0g}}$ and $\Psi_{\mathbf{g\bar{g}}}$ overlapped; the CCD camera was now conjugate to the interference plane. As shown in figure 4.1(f), I observed interference fringes with a period of 0.32 nm within the overlap spot. This image was taken by overfocusing the beam to a diameter of 80 nm, so that the beam diameter and $\alpha$ were at their designed values. Since the fringe contrast was quite low ( <20 %), I used the Fourier transform of the live image (inset, figure 4.1(f)) to monitor the appearance of the fringes. The presence of a single set of spots in the Fourier transform (corresponding to $\mathbf{g} = (\bar{1}\bar{1}1)$) confirmed that these fringes were formed due to the interference between $\Psi_{\mathbf{0g}}$ and $\Psi_{\mathbf{g\bar{g}}}$. The fringe images were captured with an exposure time between 1 and 5 seconds. Longer exposures lead to blurring due to mechanical vibrations in the sample stage, while shorter exposures result in poor signal-to-noise ratio.

## 4.3 Properties of the interference fringes

This section discusses alternative explanations for the interference fringes and lists some of their coherence characteristics.

### 4.3.1 Other possible sourced of fringes

The observed fringe spacing of 0.32 nm would also be seen in fringes produced by Talbot self-imaging[57, 1]. However the separation between the two gratings is $\sim$ 250 times the Talbot length $z_T$ for the $(\bar{1}\bar{1}1)$ lattice planes of silicon ($z_T = 2a^2/\lambda_{\text{electron}} = 82$ nm for 200 kV electrons), which makes Talbot fringes unlikely. A Moiré deflectometer would also produce

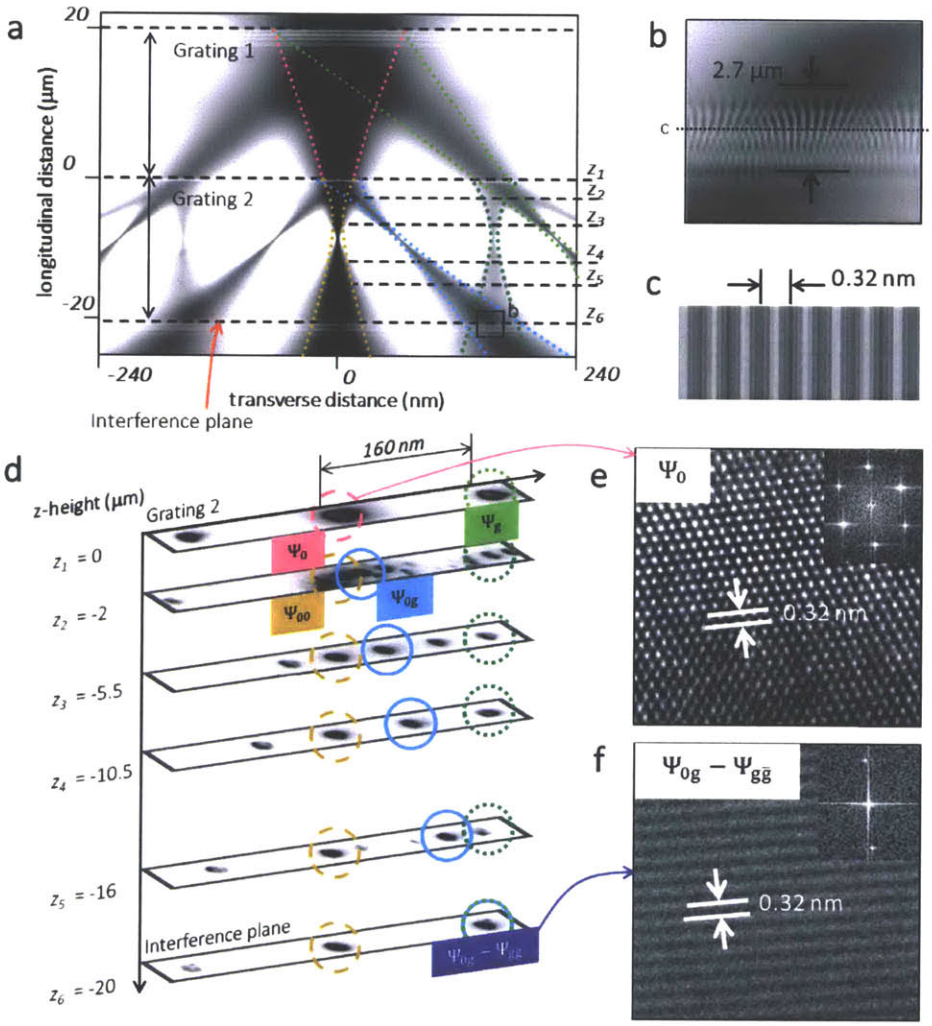
a
20
0
-20
longitudinal distance (μm)
Grating 1
Grating 2
$z_1$
$z_2$
$z_3$
$z_4$
$z_5$
$z_6$
b
-240
0
240
transverse distance (nm)
Interference plane
b
2.7 μm
c
c
0.32 nm
d
160 nm
z-height (μm)
Grating 2
$z_1$ = 0
$z_2$ = -2
$z_3$ = -5.5
$z_4$ = -10.5
$z_5$ = -16
$z_6$ = -20
$\Psi_0$
$\Psi_g$
$\Psi_{00}$
$\Psi_{0g}$
Interference plane
$\Psi_{0g} - \Psi_{g\bar{g}}$
e
$\Psi_0$
0.32 nm
f
$\Psi_{0g} - \Psi_{g\bar{g}}$
0.32 nm

Figure 4.1 *(previous page)*: Electron interferometry with the 20 µm gap interferometer.(a) GSM simulation of diffraction from the 20 µm interferometer. The black dashed lines represent the imaging planes at different stage heights $z$. In the interference plane, the two beams $\Psi_{\mathbf{0g}}$ and $\Psi_{\mathbf{g\bar{g}}}$ overlap. (b) Magnified view of the region around the interference plane as indicated in (a). For a spatial coherence length equal to 20 % of the beam diameter, the interference fringes extend for $\sim$ 2.7 µm along the optical axis. The contrast seen in this image is caused by undersampling of the actual interference fringes as explained in the text. (c) Magnified cross-section of the overlapping beams at the interference plane as indicated in (b), showing fringes with the periodicity of the $(\bar{1}\bar{1}1)$ planes, 0.32 nm. (d) ($z_1$ = 0) $\Psi_{\mathbf{0}}$ (center, pink circle), $\Psi_{\mathbf{g}}$ (right, light green circle) and $\Psi_{\bar{\mathbf{g}}}$ (left) diffracted beams on the second grating. ($z_2$ = -2 µm) $\Psi_{\mathbf{0g}}$ (circled in blue) separates out from $\Psi_{\mathbf{00}}$ (circled in yellow). $\Psi_{\mathbf{g\bar{g}}}$ is circled in dark green on the right. ($z_3$ = -5.5 µm , $z_4$ =-10.5 µm and $z_5$ = -16 µm) $\Psi_{\mathbf{0g}}$ moves towards $\Psi_{\mathbf{g\bar{g}}}$. ($z_6$ = - 20 µm) The two beams $\Psi_{\mathbf{0g}}$ and $\Psi_{\mathbf{g\bar{g}}}$ overlap and interfere.(e) TEM micrograph of the lattice of the second grating from the $\Psi_{\mathbf{0}}$ beam at $z_1$=0. (f) TEM micrograph of fringes from the interference of $\Psi_{\mathbf{0g}}$ and $\Psi_{\mathbf{g\bar{g}}}$ beams at $z_6$ = -20 µm with a period 0.32 nm. The inset shows the Fourier transform of the image. Only one set of points (corresponding to $\mathbf{g}=(\bar{1}\bar{1}1)$) are seen around the central spot, confirming the origin of the fringes.

fringes of the same period, but the direct imaging method which showed the separation and overlap of diffracted beams, along with the measurement of beam coherence, made this explanation unlikely too. Thus, the observed fringes could be attributed to coherent overlap between the diffracted beams in a Mach-Zehnder geometry.

### 4.3.2 Spatial coherence of the interfering beams

Unlike the lattice fringes from the second grating, the interference fringes shows only one orientation since they are formed by overlap between two beams ($\Psi_{\mathbf{0g}}$ and $\Psi_{\mathbf{g\bar{g}}}$). The distance along the optical axis over which the fringes persist $\Delta z$ is proportional to the spatial coherence length of the beam, which can be interpreted as the diameter of a disk of points in the beam that have a fixed mutual phase relationship. The wider this disk, the greater the extent of coherent interference along the optical axis and thus the larger is $\Delta z$. In my experiment $\Delta z \sim 3\,\mu\text{m}$. This value is close to the theoretical estimate of $2.7\,\mu\text{m}$ as shown in figure 4.1(b), which supports the assumption of the spatial coherence length of the beam in the simulation.

### 4.3.3 Sources of contrast reduction and misalignment

The maximum fringe contrast observed was 15%, similar to the contrast for the fringes at the BFP described in Chapter 3. For two interfering beams of equal amplitude the fringe contrast is ideally equal to the degree of coherence. However as can be seen from the images at $z4$ and $z5$ in figure 4.1(d), the intensities of the $\Psi_{\mathbf{0g}}$ and $\Psi_{\mathbf{g\bar{g}}}$ beams was quite different. The ratio of the average intensity of the two beams from the image at $z4$ was 0.38. Tilting to the two-beam condition is a possible solution to enhancing the intensities of the interfering beams and thus improving contrast; however the slight misalignment between the two gratings noted earlier was sufficient to prevent me from achieving the two-beam condition simultaneously for both crystals. This misalignment is expected to be due to small bending of the crystals during fabrication. Another possible source of misalignment is the rotation of the electrons

in the objective lens pre-field in which the sample is immersed.

Due to bending and variations in thickness in each of the two gratings, the relative intensities of the diffracted beams varied with translation in the plane of the gratings (the $x$-$y$ plane). Since translation along the optical axis ($z$) lead to small movement in the $x$-$y$ plane, the intensities of the beams changed as I translated the stage from the plane of the second grating to the interference plane. This change in intensity can be seen in the reduction of the intensity of the $\Psi_{\bar{\mathbf{g}}}$ spot between the images at $z_1$ and $z_2$ in figure 4.1(d).

# Chapter 5

# Conclusions and future work

In this chapter I discuss scaling of the interferometer to larger dimensions and number of gratings, and possible applications.

## 5.1 Controlling the geometry of the interferometer

This interferometer design can easily be scaled to larger gaps and numbers of gratings, which would facilitate its use in potential interferometry and holography setups by simplifying the placement of a sample and application of a field differential between the two beams. Figure 5.1(a) shows a fabricated structure with 50 µm gap between the gratings. I am currently limited by the thickness of commercially available TEM grids. Figure 5.1(b) shows a three-grating structure with different lateral area of each grating which allowed me to study diffraction through one, two or three gratings separately. Figure 5.1(c) shows a five-grating structure with 1.2 µm gap between the gratings, demonstrating control over the number of gratings in our fabricated structures. Figures 5.1(d) and (e) show convergent beam diffraction from the grating structures in figures 5.1(b) and (c) respectively, again showing multiple closely-spaced spots, as discussed for the two-grating structure.

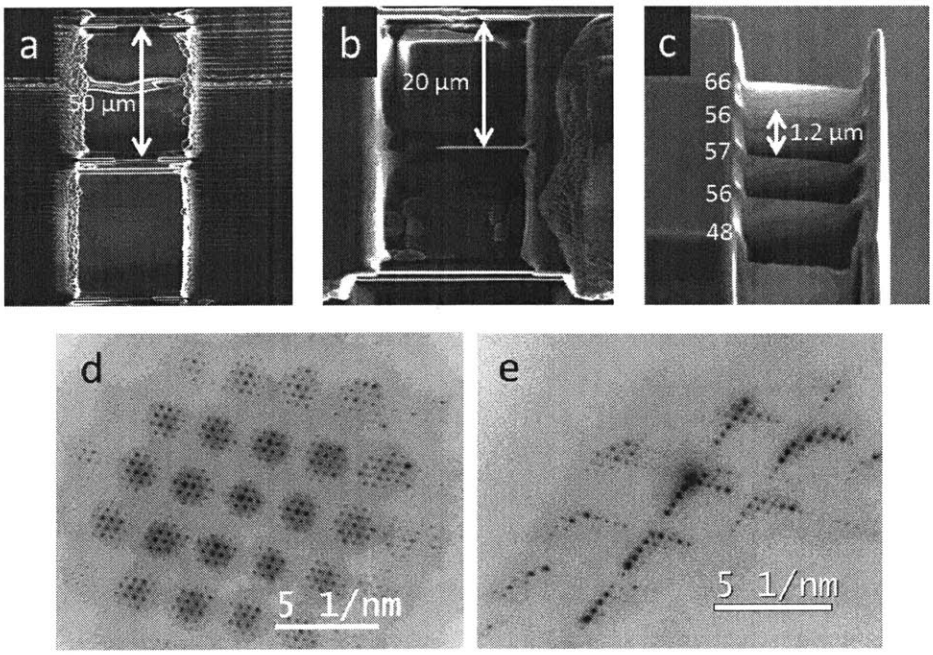


Figure 5.1: Controlling the geometry of the grating interferometers. Side-view SEM micrographs of three-grating structure with (a) 50 and (b) 20 µm gap between the gratings, showing control over the gap and lateral area of each grating respectively. (c) 52°-tilt SEM micrograph of five grating structure with 1.2 µm gap between the gratings, showing control over the number of gratings The thickness of each grating (in nm) is indicated. (d) Convergent-beam diffraction pattern from structure in (b). (e) Convergent-beam diffraction pattern from structure in (c).

## 5.2 Three-grating interferometer

Although I fabricated a three-grating interferometer to attempt a Marton-type experiment[8], the interpretation of the was hindered by contrast fluctuations, potentially caused by bending, thickness variation, or stresses in each grating. In addition to interference effects, the intensity of each diffracted beam was also affected by the thickness of each grating. The difficulty in determining the exact thickness at every point of each grating made it challenging to separate this effect from the interference. This issue can be addressed by fabricating very thin ($\sim$ 10 nm) gratings to suppress dynamical diffraction effects. In the two-grating results described earlier, this problem was circumvented by replacing the third grating with a screen on which the interference was imaged.

## 5.3 Potential applications and future work

The most immediate application of this interferometer design that will be explored is interaction-free measurement, as outlined in Chapter 1.

### 5.3.1 Application to interaction-free measurement

The separation of paths on the second grating makes it feasible to place an object in the path of one of the beams and which may allow the implementation of Elitzur and Vaidman's scheme for interaction-free imaging with electrons [41, 45]. For this demonstration, a three grating interferometer would be required. A simple object, such as a small deposit of platinum on one of the gratings, could then potentially be imaged with reduced damage. Careful design of the interferometer beam parameters and placement of the object would be required, to ensure that the object is in the path of only one beam. The gratings can also be configured in order to implement multiple and repeated quantum interrogation of distinct absorbing objects[43, 58]. An important requirement for such structures would be that the error in positioning of each grating ($\sim$ 100 nm as noted earlier) be smaller than $\Delta z$, to en-

sure coherent interference on each grating. This requirement was met by my interferometer design. A major challenge that will need to be addressed is the variations in thickness of each grating which would make interpretation of any which-path experiment difficult.

### 5.3.2 Other applications

This interferometer design is self-aligned, configurable, and scalable to larger dimensions and opens up the possibility of electron interferometry and holography in a conventional TEM with no modification of the optical column or sample holder. This grating interferometer could also be incorporated into a specially-designed electron-optic column for specific applications.

# Chapter 6

# Bibliography


[1] A. D. Cronin, J. Schmiedmayer, and D. E. Pritchard, "Optics and interferometry with atoms and molecules," *Reviews of Modern Physics*, vol. 81, no. 3, pp. 1051–1129, 2009.

[2] Q. Ru, "Incoherent electron holography," *Journal of Applied Physics*, vol. 77, no. 4, p. 1421, 1995.

[3] T. G. P., "Diffraction of Cathode Rays by a Thin Film," *Nature*, vol. 119, p. 890, 1927.

[4] C. J. Davisson and L. H. Germer, "Reflection of Electrons by a Crystal of Nickel," *Proceedings of the National Academy of Sciences of the United States of America*, vol. 14, pp. 317–322, 1928.

[5] D. Gabor, "A New Microscopic Principle," *Nature*, vol. 161, pp. 777–778, 1948.

[6] L. Marton, "Electron interferometer," *Physical Review*, vol. 85, no. 6, pp. 1057–1058, 1952.

[7] L. Marton, J. A. Simpson, and J. A. Suddeth, "Electron Beam Interferometer," *Physical Review*, vol. 90, pp. 490–491, 1953.

[8] L. Marton, J. A. Simpson, and J. A. Suddeth, "An Electron Interferometer," *Review of Scientific Instruments*, vol. 25, no. 11, pp. 1099–1104, 1954.

[9] F. Zhou, "The principle of a double crystal electron interferometer," *Journal of Electron Microscopy*, vol. 50, no. 5, pp. 371–376, 2001.

[10] G. Möllenstedt and H. Düker, "Beobachtungen und messungen an biprisma-interferenzen mit elektronenwellen," *Zeitschrift für Physik*, vol. 145, p. 377, 1956.

[11] A. V. Crewe, D. N. Eggenberger, J. Wall, and L. M. Welter, "Electron gun using a field emission source," *Review of Scientific Instruments*, vol. 39, no. 4, pp. 576–583, 1968.

[12] H. Lichte and M. Lehmann, "Electron Holography-basics and applications," *Reports on Progress in Physics*, vol. 71, p. 016102, 2008.

[13] J. M. Cowley, "Twenty forms of electron holography," *Ultramicroscopy*, vol. 41, pp. 335–348, 1992.

[14] D. Williams and C. Carter, *Transmission Electron Microscopy: A Textbook for Materials Science*. New York: Springer, 2009.

[15] A. Tonomura, N. Osakabe, T. Matsuda, T. Kawasaki, J. Endo, S. Yano, and H. Yamada, "Evidence for aharonov-bohm effect with magnetic field completely shielded from electron wave," *Phys. Rev. Lett.*, vol. 56, pp. 792–795, Feb 1986.

[16] R. E. Dunin-Borkowski, M. R. McCartney, R. B. Frankel, D. A. Bazylinski, M. Pósfai, and P. R. Buseck, "Magnetic microstructure of magnetotactic bacteria by electron holography," *Science*, vol. 282, no. 5395, pp. 1868–1870, 1998.

[17] W. C. T. Dowell and P. Goodman, "Image formation and contrast from a convergent electron beam," *Philosophical Magazine*, vol. 28, pp. 471–473, 1973.

[18] W. C. T. Dowell, "Electron interference in shadow microscopy," *Optik*, vol. 47, pp. 195–204, 1977.

[19] B. F. Buxton, G. M. Rackham, and J. Steeds, "The Dynamical Theory of a Double Crystal Interferometer," in *Ninth International Congress on Electron Microscopy, Toronto, Vol. 1*, pp. 188–189, 1978.

[20] G. M. Rackham, J. E. Loveluck, and J. W. Steeds, "A double-crystal electron interferometer," *Electron Diffraction 1927-1977 ed. P. J. Dobson, J. B. Pendry and C. J. Humphreys (London, Bristol: The Institute of Physics)*, pp. 435–440, 1977.

[21] F. Zhou, E. Plies, and M. G, "Double -crystal interferometer combined with CBED technique," *Optik*, vol. 98, no. 3, pp. 95–100, 1995.

[22] R. A. Herring, G. Pozzi, T. Tanji, and A. Tonomura, "Realization of a mixed type of interferometry using convergent-beam electron diffraction and an electron biprism," *Ultramicroscopy*, vol. 50, pp. 94–100, 1993.

[23] R. A. Herring, G. Pozzi, T. Tanji, and A. Tonomura, "Interferometry using convergent electron diffracted beams plus an electron biprism (CBED+EBI)," *Ultramicroscopy*, vol. 60, no. 1, pp. 153–159, 1995.

[24] Q. Ru, N. Osakabe, J. Endo, and A. Tonomura, "Electron holography available in non-biprism transmisson electron microscope," *Ultramicroscopy*, vol. 53, pp. 1–7, 1993.

[25] B. M. Mertens, M. H. F. Overwijk, and P. Kruit, "Off-axis holography with a crystal beam splitter," *Ultramicroscopy*, vol. 77, no. 1-2, pp. 1–11, 1999.

[26] C. Jönsson, "Elektroneninterferenzen an mehreren künstlich hergestellten Feinspalten," *Zeitschrift fur Physik*, vol. 161, pp. 454–474, Aug. 1961.

[27] Y. Ito, A. Bleloch, J. Paterson, and L. Brown, "Electron diffraction from gratings fabricated by electron beam nanolithography," *Ultramicroscopy*, vol. 52, no. 3, pp. 347 – 352, 1993.

[28] Y. Ito, A. Bleloch, and L. Brown, "Nanofabrication of solid- state fresnel lenses for electron optics," *Nature*, vol. 394, pp. 49 – 52, 1998.

[29] G. Gronniger, B. Barwick, H. Batelaan, T. Savas, D. Pritchard, and A. D. Cronin, "Electron diffraction from free-standing, metal-coated transmission gratings," *Applied Physics Letters*, vol. 87, no. 12, pp. 1–3, 2005.

[30] G. Gronniger, B. Berwick, and H. Batelaan, "A three-grating electron interferometer," *New Journal of Physics*, vol. 8, 2006.

[31] R. Bach, G. Gronniger, and H. Batelaan, "An electron Talbot-Lau interferometer and magnetic field sensing," *Applied Physics Letters*, vol. 103, no. 25, pp. 1–5, 2013.

[32] J. Verbeeck, H. Tian, and P. Schattschneider, "Production and application of electron vortex beams.," *Nature*, vol. 467, no. 7313, pp. 301–304, 2010.

[33] B. J. McMorran, A. Agrawal, I. M. Anderson, A. a. Herzing, H. J. Lezec, J. J. McClelland, and J. Unguris, "Electron vortex beams with high quanta of orbital angular momentum.," *Science (New York, N.Y.)*, vol. 331, no. 6014, pp. 192–195, 2011.

[34] S. Frabboni, G. C. Gazzadi, and G. Pozzi, "Young's double-slit interference experiment with electrons," *American Journal of Physics*, vol. 75, no. 11, pp. 1053–1055, 2007.

[35] S. Frabboni, G. C. Gazzadi, and G. Pozzi, "Nanofabrication and the realization of feynman's two-slit experiment," *Applied Physics Letters*, vol. 93, no. 7, 2008.

[36] S. Frabboni, C. Frigeri, G. C. Gazzadi, and G. Pozzi, "Two and three slit electron interference and diffraction experiments," *American Journal of Physics*, vol. 79, no. 6, p. 615, 2011.

[37] S. Frabboni, A. Gabrielli, G. C. Gazzadi, F. Giorgi, G. Matteucci, G. Pozzi, N. S. Cesari, M. Villa, and A. Zoccoli, "The young-feynman two-slits experiment with single

electrons: Build-up of the interference pattern and arrival-time distribution using a fast-readout pixel detector," *Ultramicroscopy*, vol. 116, pp. 73 – 76, 2012.

[38] S. Frabboni, G. C. Gazzadi, V. Grillo, and G. Pozzi, "Elastic and inelastic electrons in the double-slit experiment: A variant of Feynman's which-way set-up," *Ultramicroscopy*, vol. 154, pp. 49–56, 2015.

[39] R. Bach, D. Pope, S.-H. Liou, and H. Batelaan, "Controlled double-slit electron diffraction," *New Journal of Physics*, vol. 15, no. 3, p. 033018, 2013.

[40] G. F. Missiroli, G. Pozzi, and U. Valdre, "Electron interferometry and interference electron microscopy," *Journal of Physics E: Scientific Instruments*, vol. 14, p. 649, 1981.

[41] A. Elitzur and L. Vaidman, "Quantum mechanical interaction-free measurements," *Foundations of Physics*, vol. 23, p. 987, 1993.

[42] A. White, J. Mitchell, O. Nairz, and P. Kwiat, ""Interaction-free" imaging," *Physical Review A*, vol. 58, pp. 605–613, jul 1998.

[43] P. Kwiat, H. Weinfurter, T. Herzog, A. Zeilinger, and M. A. Kasevich, "Interaction-Free Measurement," *Physical Review Letters*, vol. 74, no. June, pp. 4763–4766, 1995.

[44] W. Putnam and M. Yanik *Physical Review A*, vol. 80, p. 040902(R), 2009.

[45] P. Kruit, R. G. Hobbs, C.-S. Kim, Y. Yang, V. R. Manfrinato, J. Hammer, S. Thomas, P. Weber, B. Klopfer, C. Kohstall, T. Juffmann, M. A. Kasevich, P. Hommelhoff, and K. K. Berggren, "Designs for a quantum electron microscope.," *Ultramicroscopy*, vol. 164, pp. 31–45, 2016.

[46] R. Erni, M. D. Rossell, C. Kisielowski, and U. Dahmen, "Atomic-resolution imaging with a sub-50-pm electron probe," *Phys. Rev. Lett.*, vol. 102, p. 096101, Mar 2009.

[47] M. Misra and R. Egerton *Ultramicroscopy*, vol. 15, pp. 337–344, 1984.

[48] R. Glaeser *Nature Methods*, vol. 13, pp. 28–32, 2016.

[49] H. Khatter, A. G. Myasnikov, S. K. Natchiar, and B. P. Klaholz *Nature*, vol. 520, pp. 640–645, 2015.

[50] B. Mertens and P. Kruit, "Results of a pilot experiment on direct phase determination of diffracted beams in TEM," in *Electron Microscopy and Analysis Group Conf. EMAG99, Sheffield*, pp. 133–136, 1999.

[51] J. A. Simpson, "The theory of the three-cyrstal electron interferometer," *Rev. Sci. Instrum.*, vol. 25, no. 11, p. 1105, 1954.

[52] A. T. Freiberg and R. J. Sudol, "Propogation Parameters of Gaussian Schell-Model Beams," *Optics Communications*, vol. 41, no. 6, pp. 383–387, 1982.

[53] B. McMorran and A. Cronin, "Gaussian Schell Source as Model for Slit-Collimated Atomic and Molecular Beams," *e-print arXiv:0804.1162v1*, 2008.

[54] B. McMorran and A. D. Cronin, "Model for partial coherence and wavefront curvature in grating interferometers," *Physical Review A - Atomic, Molecular, and Optical Physics*, vol. 78, no. 1, pp. 1–10, 2008.

[55] R. Dronyak, K. S. Liang, Y. P. Stetsko, T. K. Lee, C. K. Feng, J. S. Tsai, and F. R. Chen, "Electron diffractive imaging of nano-objects using a guided method with a dynamic support," *Applied Physics Letters*, vol. 95, no. 11, p. 111908, 2009.

[56] S. Morishita, J. Yamasaki, and N. Tanaka, "Measurement of spatial coherence of electron beams by using a small selected-area aperture," *Ultramicroscopy*, vol. 129, pp. 10–17, 2013.

[57] B. J. McMorran and A. D. Cronin, "An electron Talbot interferometer," *New Journal of Physics*, vol. 11, p. 033021, 2009.

[58] J. Wang, K. Pitt, and M. Milgie, "Multiple interferometer interaction free measurement using polarized light," *Journal of Physics B: Atomic, Molecular and Optical Physics*, vol. 49, no. 4, p. 045501, 2016.